Kinetochore- and chromosome-driven transition of microtubules into bundles promotes spindle assembly

Jurica Matković[1], Subhadip Ghosh[2], Mateja Ćosić[1], Nenad Pavin[2], Iva M. Tolić[1*]

[1]Division of Molecular Biology, Ruđer Bošković Institute, Bijenička cesta 54, 10000 Zagreb, Croatia
[2]Department of Physics, Faculty of Science, University of Zagreb, Bijenička cesta 32, 10000 Zagreb, Croatia

*Correspondence to: tolic@irb.hr

ABSTRACT

Mitotic spindle assembly is crucial for chromosome segregation and relies on bundles of microtubules that extend from the poles and overlap in the middle. However, how these structures form remains poorly understood. Here we show that overlap bundles arise through a network-to-bundles transition driven by kinetochores and chromosomes. STED super-resolution microscopy revealed that PRC1-crosslinked microtubules initially form loose arrays, which become rearranged into bundles. Kinetochores promote microtubule bundling by lateral binding via CENP-E/kinesin-7 in an Aurora B-regulated manner. Bundle separation is driven by steric interactions of the bundle-associated chromosomes at the spindle midplane since spindles with uncondensed or uncongressed chromosomes are narrower. In agreement with experiments, theoretical modeling suggests that bundles arise through competing attractive and repulsive mechanisms. Finally, perturbation of overlap bundles led to inefficient correction of erroneous kinetochore-microtubule attachments. Thus, kinetochores and chromosomes drive coarsening of a uniform microtubule array into overlap bundles, which promote not only spindle formation but also chromosome segregation fidelity.

INTRODUCTION

Segregation of chromosomes during mitosis relies on the mitotic spindle, a supramolecular micro-machine made of microtubules and numerous microtubule-associated proteins, which is built de novo in each cell cycle[1]. While some spindle microtubules exist as individual filaments, such as astral microtubules, many are organized in bundles, such as kinetochore fibers and overlap bundles[2,3]. Kinetochore fibers are bundles of parallel microtubules that attach in an end-on manner to the kinetochore on the centromere of each chromosome, and link the kinetochore with the spindle pole[4,5]. Overlap or interpolar bundles consist of antiparallel microtubules that extend from the opposite spindle halves[6]. Spindle assembly has been extensively studied with focus on kinetochore dynamics and the formation of kinetochore fibers[7–12], whereas the mechanism of overlap bundle formation remains poorly understood.

Overlap bundles are essential for spindle assembly, as inhibition of the Eg5/kinesin-5 motor protein, which slides apart the antiparallel microtubules within the bundle, leads to monopolar spindles[13–16]. Such spindles without overlap bundles cannot segregate the chromosomes even though they usually contain kinetochore fibers, highlighting the indispensable role of overlap bundles in spindle functioning. In a mature spindle in metaphase, overlap bundles link sister kinetochore fibers like a bridge and because of this interaction are known as bridging fibers[17]. Their functions include balancing the tension on kinetochores[17–21], promoting chromosome alignment at the spindle midplane[22,23] and driving spindle elongation and chromosome segregation in anaphase[24–28]. Microtubules within bridging fibers are linked by the protein regulator of cytokinesis 1 (PRC1)[17,21,29], a crosslinker that has a 10-fold preference for antiparallel versus parallel microtubule overlaps *in vitro*[30–33]. Such crosslinkers together with motor proteins may drive the formation of initial overlaps between two antiparallel microtubules, as shown by computer simulations[34–37].

Mitotic spindles of human cells are made of more than 6000 microtubules[38]. In general, microtubules present in large numbers can exist in different phases, from loose networks to tight bundles, where the networks can be isotropic if the filaments are unoriented, nematic if the filaments are parallel and point either way, or polar if they point in a common direction[39]. Different types of microtubule networks have been studied in vitro[40–42], together with theoretical studies that explored under what conditions certain types of polymer networks appear or undergo a transition to bundles[43–47]. Yet, whether similar transitions occur in cells and what biological function they may have are open questions.

In this work we develop an assay for bundle formation, together with a theoretical model, and show that microtubules crosslinked by PRC1 undergo a network-to-bundles transition during early stages of spindle assembly. We find that this transition is stimulated by kinetochores, which promote microtubule bundling by binding to them laterally via CENP-E in a manner regulated by Aurora B. We further show that the separation of the bundles, which leads to spindle widening and the characteristic spindle shape, is driven by steric interactions of the chromosomes bound to the bundles as they congress to the spindle midplane, based on our findings that spindles with uncondensed or incompletely congressed chromosomes are narrower. Moreover, we identify a function of overlap bundles in the correction of erroneous kinetochore-microtubule attachments. Our work thus reveals that kinetochores and chromosomes together with crosslinkers drive coarsening of an initially uniform microtubule array into neatly organized overlap bundles, which not only support spindle assembly but also promote error-free mitosis.

RESULTS

The network of PRC1-crosslinked microtubules undergoes a transition to bundles

The overarching question of how the cell generates microtubule bundles that form the spindle shape contains two parts: how individual bundles are formed and what determines their separation. To study individual bundle formation, we first explored microtubule organization during early stages of mitosis by using stimulated emission depletion (STED) microscopy[48] to obtain super-resolution images of microtubules, together with the microtubule crosslinker PRC1 and chromosomes (Fig. 1a). The spatial pattern of microtubules and PRC1 changed profoundly during spindle formation and maturation (Fig. 1a). In early prometaphase characterized by the "prometaphase rosette" where the chromosomes are arranged like flower petals along the edge of the nascent spindle[49,50], the majority of spindle body microtubules appeared as a diffuse array with a few bundles present mainly at the edges ("Rosette" in Fig. 1a and Extended Data Fig. 1a). During late prometaphase, when chromosomes increasingly congress to the equatorial plane, and afterwards in metaphase, additional microtubule bundles appeared and their spacing became more regular, which was accompanied by the appearance of PRC1 stripes along the bundles ("Congression" and "Metaphase" in Fig. 1a and Extended Data Fig. 1a).

101 By looking at cross-sections of vertically oriented spindles, we found that microtubules
102 of the spindle body are initially uniformly distributed over a ring-shaped region, and astral
103 microtubules extend radially outwards (Fig. 1a end-on view). The spindle body microtubules
104 became rearranged into discrete bundles that fill the spindle cross-section at an even spacing
105 (end-on view in Fig. 1a and Extended Data Fig. 1a). Similarly, PRC1 distribution changed from
106 a nearly homogeneous scattering over the ring-shaped region, which we call PRC1 network, to
107 spot-like structures that colocalized with the microtubule bundles (end-on view in Fig. 1a and
108 Extended Data Fig. 1a).

109 To study how a loose microtubule array transforms into bundles, we developed a live-
110 cell assay termed "bundling assay" based on PRC1 as a marker of microtubule overlaps, where
111 we imaged cross-sections of vertically oriented spindles in HeLa cells expressing PRC1-GFP
112 starting at the rosette stage for 10 minutes (Fig. 1b). The rosette was identified by a
113 chromosome circle surrounding the spindle, which was not yet fully closed (Extended Data
114 Fig. 1b top and Fig. 1a bottom left). Time-lapse images revealed that the spatial distribution of
115 PRC1 in the spindle cross-section gradually changes from a homogeneous dispersion over a
116 ring-shaped area (PRC1 network) to discrete clusters (Fig. 1b and Supplementary Video 1), in
117 agreement with STED images of fixed cells. Segmentation analysis (Methods; Extended Data
118 Fig. 1c,d) showed that the number of PRC1-labeled segments and their mean PRC1-GFP
119 intensity increased over time, whereas the segment area decreased (Fig. 1c,d and Extended
120 Data Fig. 1e).

121 Intensity profiles of PRC1 along the ring-shaped area indicate that in comparison with
122 the nearly constant PRC1 intensity in the rosette, the intensity at a later stage exhibited higher
123 peaks and deeper valleys (t=0 vs. 7.2 minutes, Fig. 1e,f). The mean intensity did not change
124 substantially, but the standard deviation increased 2.6-fold (n=10, Fig. 1g and Extended Data
125 Fig. 1f). This suggests that the nearly uniform PRC1-labeled microtubule network undergoes
126 a transition to bundles that accumulate PRC1, leaving the space between the bundles almost
127 free from PRC1.

128 We next asked how the initial PRC1 network is formed. A large fraction of spindle
129 microtubules is nucleated by the augmin complex at the wall of other microtubules[51,52]. When
130 we used the bundling assay on cells depleted of the augmin subunit Haus6, we found that, in
131 contrast to untreated cells, a PRC1 network was absent at the rosette stage (Extended Data Fig.
132 1g-i and Supplementary Video 2) and the dynamics of bundle formation was slower (Extended
133 Data Fig. 1j-l). These results suggest that the initial array of microtubules crosslinked by PRC1
134 is largely nucleated by the augmin complex.

To verify that the redistribution of PRC1 indeed reflects changes of the microtubule network, which was observed in STED images, we first used nocodazole to depolymerize microtubules at the rosette stage. This treatment caused the disappearance of the PRC1 network (Extended Data Fig. 2a), indicating that PRC1 forming this structure is bound to microtubules. Second, we noticed that PRC1 colocalized with microtubules in the central part of the spindle but was excluded from astral microtubules throughout prometaphase (Fig. 1a and Extended Data Fig. 2b), suggesting that PRC1 selectively localizes to antiparallel microtubule overlaps already in early mitosis. Third, we imaged spindles stained with SiR-tubulin and found that, similarly to PRC1, tubulin signal undergoes a change from a nearly uniform to a spotted distribution (Extended Data Fig. 2c,d). Yet, PRC1 is a better marker of antiparallel overlaps not only because of its specificity but also because of the lower background signal (Fig. 1b vs. Extended Data Fig. 2c). Moreover, an increase in the number of bundles during prometaphase was observed in horizontally oriented HeLa spindles labeled with PRC1-GFP, as well as in spindles of human non-transformed retinal pigment epithelial hTERT-RPE1 cells stained with SiR-tubulin (Extended Data Fig. 2e), suggesting that the process of bundle formation is independent of the cell line and labeling. Taken together, these results confirm that the PRC1 redistribution reflects the redistribution of overlap microtubules from a nearly uniform network in early prometaphase to the regularly spaced overlap bundles in metaphase.

Figure 1

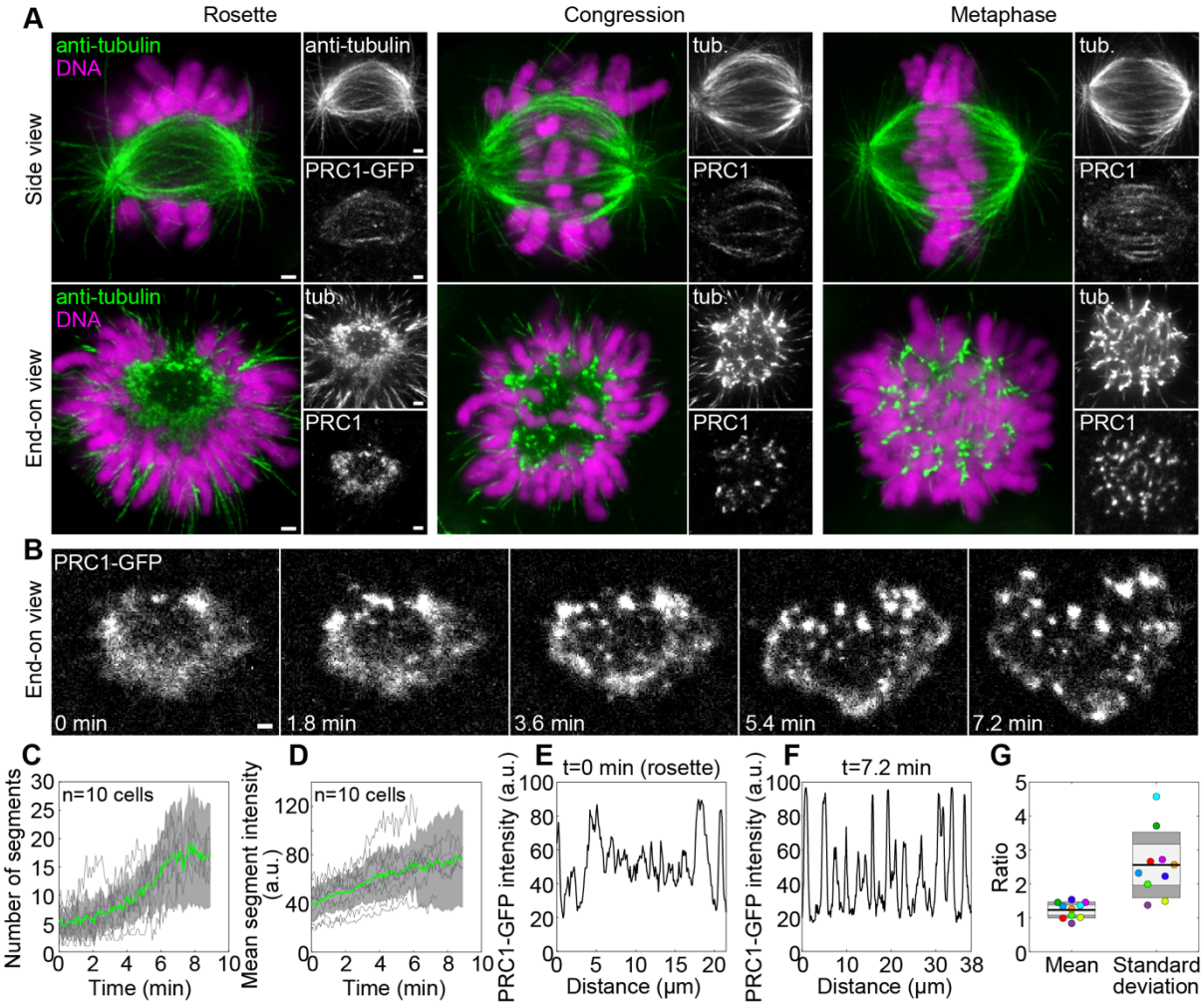

Fig. 1: PRC1-crosslinked microtubules undergo a transition from a loose array to bundles during spindle assembly.

a, Spindles immunostained for α-tubulin and imaged at STED resolution in a HeLa-Kyoto BAC cell line stably expressing PRC1-GFP with DNA stained by DAPI (both imaged at a confocal resolution), in early prometaphase ("Rosette"), late prometaphase ("Congression"), and metaphase. Spindles lying parallel (first row) or perpendicular (second row) to the imaging plane are shown. **b**, Time lapse images (single plane) of a cross-section of a vertically oriented prometaphase spindle in a HeLa-Kyoto BAC cell stably expressing PRC1-GFP, starting with the prometaphase rosette. **c**, Number of PRC1 segments in the midplane over time for cells as in panel **b**, obtained using Squash segmentation. Gray lines represent individual cells, green line the mean and gray areas the standard deviation, n=10 cells in 10 independent experiments. **d**, Mean intensity of PRC1 segments from the same cells as in **c**. **e**,**f**, Intensity line plots of PRC1-GFP in the cell from panel **b** at t=0 (**e**) and t=7.2 min (**f**) along the periphery of the spindle cross-section (lines shown in Extended Data Fig. 1f). **g,** Ratio of mean PRC1-GFP intensity in panels **f** and **e** ("Mean") and ratio of the standard deviation in panels **f** and **e** ("Standard deviation"). The black line shows the mean; the light and dark grey areas mark 95% confidence interval on the mean and

170 standard deviation, respectively; n=10 cells in 10 independent experiments. Dots of the same color represent the
171 same cells. All scale bars, 1 μm.
172
173 **Kinetochores promote overlap bundle formation by CENP-E-mediated attachments in**
174 **an Aurora B-dependent manner**
175
176 In metaphase, overlap microtubule bundles are found close to a pair of sister kinetochores[53,54].
177 This finding inspired us to ask whether kinetochores play a role in bundle formation during
178 early prometaphase (Fig. 2a), a stage when kinetochores are laterally attached to spindle
179 microtubules[49,50,55,56]. We found that, in a rosette cross-section of unperturbed spindles, most
180 of the PRC1-labeled bundles had an adjacent kinetochore at its outer side (Fig. 2b). The bundles
181 with an associated kinetochore had a higher PRC1 signal intensity than those without a
182 kinetochore (Fig. 2c), consistent with the hypothesis that kinetochores promote microtubule
183 bundling.
184 To explore the role of lateral attachments of kinetochores in bundle formation, we
185 inhibited Aurora B, which is in prometaphase localized mainly at centromeres (Extended Data
186 Fig. 3a) and required for the lateral attachment[50,57–59]. We first explored the effect of Aurora B
187 inhibition by barasertib (AZD1152-HQPA)[60,61] on mature bundles in metaphase. Strikingly,
188 we found a 4.2-fold decrease in the signal intensity of individual PRC1-labeled bundles in the
189 cross-section of metaphase spindles (n=452 bundles from 14 cells, Fig. 2d,e; Extended Data
190 Fig. 3b and side view in Extended Data Fig. 3c), suggesting that antiparallel bundles contained
191 fewer microtubules. To confirm this, we measured the tubulin signal intensity in the central
192 part of individual bridging fibers in the region between sister kinetochores in metaphase and
193 found a 7.6-fold decrease upon Aurora B inhibition (Fig. 2f,g and Extended Data Fig. 3d).
194 Thus, Aurora B activity regulates the number of microtubules within the bridging fibers in
195 metaphase.
196 We addressed the role of Aurora B from another angle by exploring localization
197 relationships between Aurora B and PRC1 in metaphase. We found that the signal intensity of
198 PRC1 within the bridging fiber is correlated with the signal of Aurora B in the neighboring
199 centromere (Extended Data Fig. 3e). Moreover, when we displaced Aurora B from the inner
200 centromere to a position closer to the kinetochore by transfecting cells with CENP-B-INCENP-
201 GFP[62–64], we observed a remarkable change in the PRC1 signal distribution. Instead of a single
202 broad PRC1 peak in the central part of the spindle that is evident in untreated cells, the cells
203 with displaced Aurora B showed two PRC1 peaks about 1 μm away from the spindle equator

204 on either side (Fig. 2h,i and Extended Data Fig. 3f). These results suggest that Aurora B
205 regulates the localization of PRC1-labeled bundles within the spindle.
206 To test the effect of Aurora B on the dynamics of bundle formation during early
207 prometaphase, we combined the bundling assay with acute inhibition of Aurora B by barasertib
208 added at the rosette stage (Fig. 2j and Supplementary Video 3). Aurora B inhibition led to a
209 slower increase in the number and intensity of PRC1-labeled bundles over time in comparison
210 with untreated cells (Extended Data Fig. 3g,h), which confirmed that Aurora B regulates the
211 dynamics of bundle formation.
212

Figure 2

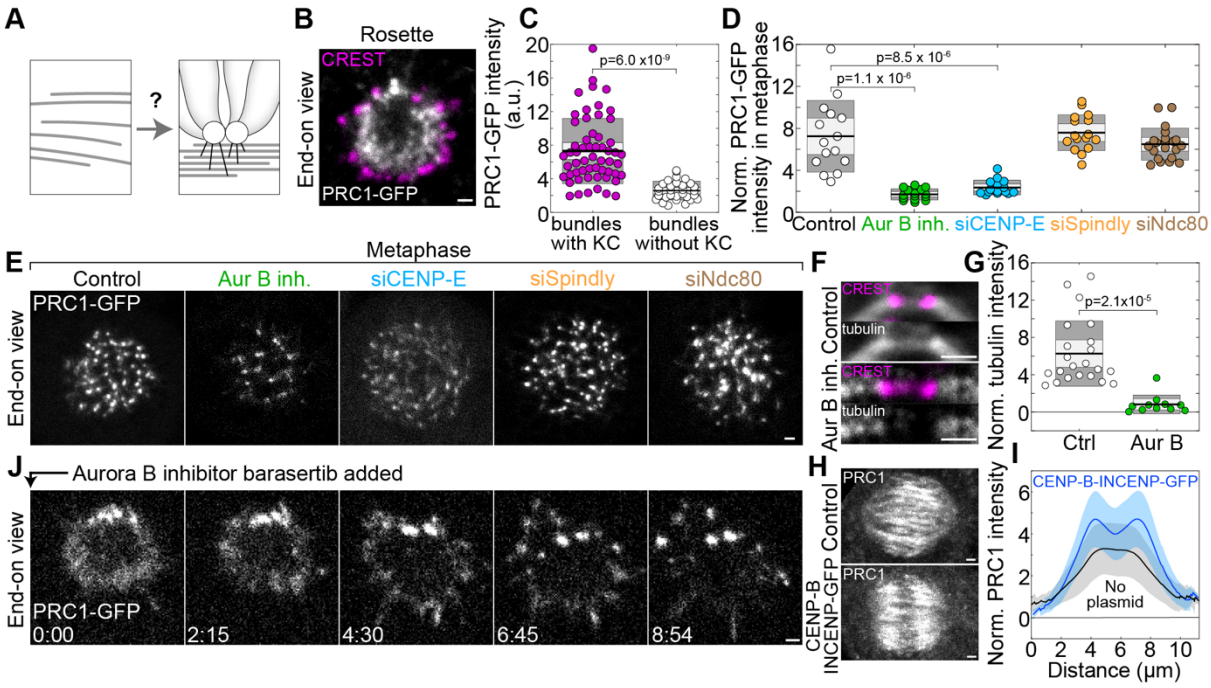

213
214
215 **Fig. 2: Kinetochores promote microtubule bundle formation in an Aurora B-dependent manner.**
216 **a**, Schematic view of kinetochore-driven overlap bundle formation. **b**, Midplane of a vertically oriented
217 prometaphase rosette immunostained for CREST (magenta) in a HeLa-Kyoto BAC cell line stably expressing
218 PRC1-GFP (white). **c**, PRC1-GFP intensity of bundles with and without adjacent kinetochore, n=57 bundles with
219 kinetochores attached and 30 without, in 10 cells from 3 independent immunostainings. **d**, PRC1-GFP intensity
220 of bundles in vertically oriented metaphase spindles, normalized to the cytoplasmic PRC1-GFP intensity. Circles
221 represent the mean bundle intensity per spindle. One-way ANOVA test showed significant difference between
222 group means, p-values are given for the significant differences from control. Numbers of bundles/cells from left
223 to right: 827/15, 452/14, 730/15, 880/16, 774/21; 3 independent experiments per condition. **e**, Images of vertically
224 oriented metaphase spindles in a HeLa-Kyoto BAC cell line stably expressing PRC1-GFP (white), treated as
225 indicated. **f**, Image of a region around a kinetochore pair immunostained for CREST (magenta) and tubulin (white)
226 in an untransfected HeLa cell, control (top) and after Aurora B inhibition (bottom). Merged channels and only

227 tubulin are shown. **g**, Mean tubulin intensity in the middle of the bridging fiber in control and Aurora B-inhibited
228 cells, normalized to the cytoplasmatic anti-tubulin intensity; n=22 bundles from 14 cells for control and 11 bundles
229 from 9 cells for Aurora B inhibition, from 3 independent immunostainings. **h**, Maximum-intensity projections of
230 41 planes of metaphase spindles immunostained for PRC1 (white) in an untransfected HeLa cell line (control, top
231 image), and cells transfected with CENP-B-INCENP-GFP (bottom image). **i**, Line intensity profiles of the anti-
232 PRC1 signal intensity, normalized to the cytoplasmatic anti-PRC1 signal intensity, along the spindle main axis,
233 for control (n=33) and treated cells as in **h** (n=30), mean (central line) and standard deviation (colored surfaces),
234 3 independent experiments per condition. **j**, Time lapse images (single plane) of a cross-section of a vertically
235 oriented prometaphase spindle in a HeLa-Kyoto BAC cell stably expressing PRC1-GFP, after addition of the
236 Aurora B inhibitor Barasertib at the prometaphase rosette stage. In **c**, **d** and **g** the black line shows the mean; the
237 light and dark grey areas mark 95% confidence interval on the mean and standard deviation, respectively. All
238 scale bars, 1 μm.
239
240 The mechanism by which Aurora B at the kinetochore promotes microtubule bundling
241 likely relies on Aurora B substrates involved in microtubule binding. We hypothesize that if
242 microtubule-binding proteins that are localized at the kinetochore in multiple copies attach to
243 several microtubules positioned close to the kinetochore, this could promote microtubule
244 bundling (Fig. 3a). Candidates for this activity are two motor proteins, CENP-E (kinesin-7)
245 and cytoplasmic dynein, and the outer kinetochore protein Ndc80, given that they bind to
246 microtubules, localize at the kinetochore in prometaphase (CENP-E and dynein) or throughout
247 mitosis (Ndc80), and are regulated by Aurora B[50,65–67].
248 We first analyzed the signal intensity of PRC1-labeled bundles in metaphase after
249 depletion of these candidates. CENP-E depletion by siRNA resulted in a 3.1-fold lower
250 intensity of PRC1 in individual bundles in metaphase (n=730 bundles from 14 cells, Fig. 2d,e
251 and Extended Data Fig. 3b,c; see Extended Data Fig. 4 for depletion efficiency) and a 2.8-fold
252 decrease in the tubulin signal intensity in the central part of individual bridging fibers (Fig.
253 3b,c and Extended Data Fig. 3d). These results suggest that CENP-E is required for proper
254 bundle formation and motivated us to explore its localization and dynamics during early
255 prometaphase. In the rosette, we found that CENP-E localizes at the side of the kinetochore
256 facing the PRC1-labeled bundles (Fig. 3d,e), which suggests that it links the kinetochore with
257 the antiparallel bundles. The bundling assay revealed that acute inhibition of CENP-E by GSK-
258 923295[68] at the rosette stage led to a slower increase in the number and intensity of PRC1-
259 labeled bundles over time than in untreated cells (Fig. 3f, Extended Data Fig. 3i,j and
260 Supplementary Video 4), supporting a role of CENP-E in bundle formation. Finally, the
261 hypothesis that CENP-E promotes bundling predicts that overexpression of CENP-E should
262 lead to increased bundling, which we indeed observed as a higher intensity of PRC1-labeled

263 bundles in metaphase upon CENP-E overexpression (Fig. 3g,h and Extended Data Fig. 3k).
264 Taken together, these results indicate that kinetochores promote bundle formation via CENP-
265 E-mediated microtubule binding.

266 To test whether dynein at the kinetochore is required for overlap bundle formation, we
267 depleted Spindly, a kinetochore-specific adaptor for dynein that recruits dynein to the
268 kinetochore[69]. Spindly depletion did not change the signal intensity of PRC1-labeled bundles
269 in metaphase (Fig. 2d,e and Extended Data Fig. 3b; see Extended Data Fig. 4 for depletion
270 efficiency), suggesting that dynein is not crucial for overlap bundle formation. Similarly,
271 Ndc80 depletion did not alter bundle intensity (Fig. 2d,e and Extended Data Fig. 2b; see
272 Extended Data Fig. 4 for depletion efficiency), arguing against a major role of Ndc80 in overlap
273 bundle formation. Moreover, as Ndc80 is required for the establishment of end-on attachments
274 of kinetochores to microtubules and thus the formation of kinetochore fibers[57,66,70,71], these data
275 imply that overlap microtubule bundles can form independently of kinetochore fibers.
276
277

Figure 3

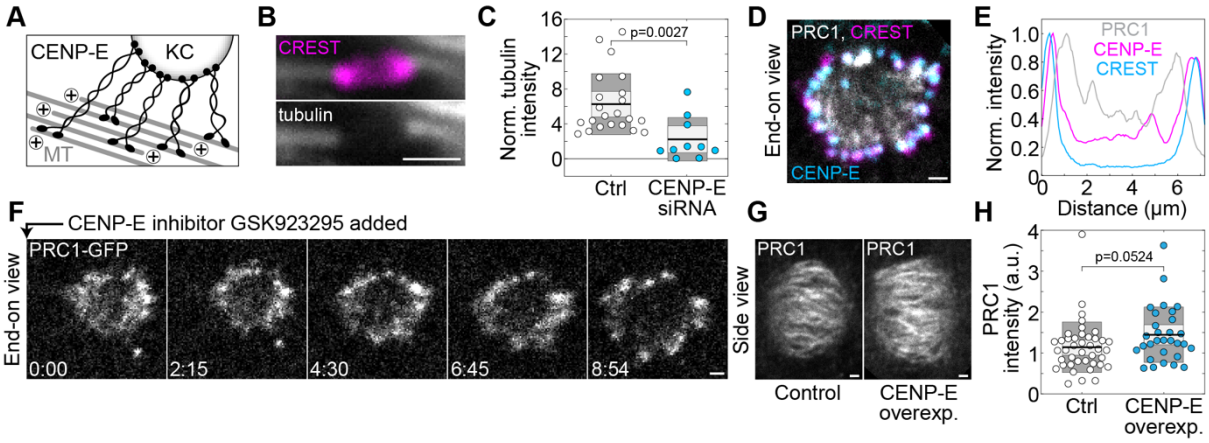

278
279
280 **Fig. 3: CENP-E promotes overlap bundle formation.**
281 **a**, Schematic view of how CENP-E may promote microtubule bundling. **b**, Image of a region close to kinetochores
282 immunostained for CREST (magenta) and tubulin (white) in a CENP-E depleted HeLa cell. **c**, Mean tubulin
283 intensity in the middle of the bridging fiber in control and CENP-E depleted cells, normalized to the cytoplasmatic
284 tubulin intensity, n=22 bundles from 14 cells for control and 10 bundles from 7 cells for CENP-E depletion, from
285 3 independent immunostainings. **d**, Cross-section of a vertically oriented prometaphase rosette immunostained
286 for CREST (magenta) and CENP-E (cyan) in a HeLa-Kyoto BAC cell line stably expressing PRC1-GFP (white).
287 **e**, Line intensity plots of PRC1-GFP, CREST and CENP-E from the spindle shown in **d**, normalized to the
288 corresponding maximum value. The line was drawn across the middle of the spindle cross-section, with a line
289 thickness of 1/3 of the spindle cross-section. **f**, Time lapse images (single plane) of a cross-section of a vertically

290 oriented prometaphase spindle in a HeLa-Kyoto BAC cell stably expressing PRC1-GFP (white), after addition of
291 the CENP-E inhibitor GSK923295 at the prometaphase rosette stage. **g**, Images of horizontally oriented metaphase
292 spindles immunostained for PRC1 (white) in an untransfected HeLa cell line (control, left) and after CENP-E
293 overexpression (right). **h**, Total PRC1 intensity on the spindle in control (n=41) and CENP-E overexpression
294 (n=30), from 3 immunostainings. In **c** and **h**, the black line shows the mean; the light and dark grey areas mark
295 95% confidence interval on the mean and standard deviation, respectively. All scale bars, 1 μm.
296
297 **Steric interactions of the chromosomes separate the bundles and expand spindle width**
298
299 As the bundles form, they undergo characteristic movements. We first focused on the bundles
300 that connect the centrosomes in a straight line, which can be identified by the highest PRC1
301 signal and a lack of an attached chromosome at the rosette stage (see Fig 1a). These bundles
302 are typically found at the edge of the rosette and become centrally positioned over a period of
303 about 5 minutes (Fig. 4a, images to the left). We traced the movement of all bundles and found
304 that, in a coordinate system centered at the brightest bundles, the bundles forming adjacent to
305 them move outwards and encircle them, whereas the bundles forming on the opposite side of
306 the cross-section move away from the brightest bundles (Fig. 4a, traces and Supplementary
307 Video 5). As this movement is accompanied by the arrival of more and more chromosomes to
308 the spindle midplane, we hypothesized that chromosomes promote bundle separation and thus
309 spindle width expansion by steric effects (crowding) upon congression to the midplane. Indeed,
310 we found that as new chromosomes arrived at the midplane, the chromosomes that were already
311 there moved away from the site of the new arrival (Fig. 4b left). This led to the overall outward
312 movement of the PRC1-labeled bundles and spindle widening (Fig. 4b right and Supplementary
313 Video 6). When looking at the spindles in a side view, we found that the spindle width increases
314 as increasingly more chromosomes arrive to the metaphase plate (Fig. 4c,d and Supplementary
315 Video 7). These results support the hypothesis that chromosome crowding increases bundle
316 separation.
317 This hypothesis predicts that removing the chromosomes from the spindle and/or
318 decondensing the chromatin should result in narrower spindles. To test this idea, we induced
319 mitosis with unreplicated genome (MUG) by treating the cells with hydroxyurea to inhibit
320 DNA replication and caffeine to override the DNA damage checkpoint[10,72], because in such
321 cells the bulk of the uncondensed chromatin remains away from the spindle, while the
322 kinetochores are attached to the spindle microtubules[10]. We found that the MUG spindles were
323 significantly narrower with more tightly packed bundles than spindles in untreated cells (Fig.
324 4e,f).

Another prediction of the chromosome crowding hypothesis is that if the chromosomes are not aligned at the equator but distributed over the spindle, the spindles should be narrower, which we tested by several protein depletions. Ndc80 depletion, which results in a large fraction of chromosomes distributed along the spindle due to the absence of kinetochore fibers[70,73,74], led to narrower spindles than in untreated cells (Fig. 4e,f). To test chromosome misalignment without abolishing kinetochore fibers, we used depletion of Kif18A (kinesin-8), a motor protein that regulates chromosome oscillations around the spindle midplane, whose depletion leads to extensive oscillations and hence chromosome scattering along the spindle[75,76]. In this case we also found narrower spindles[77](Fig. 4f). To further test our hypothesis, we divided the cells depleted of CENP-E into two groups: those with high chromosome misalignment, where more than 50% of the total chromosome mass was found away from the spindle midplane, and low misalignment where 1-5 chromosomes were misaligned. CENP-E depleted spindles with high misalignment were narrower than those with low misalignment (Fig. 4e,f). Taken together, these results support the hypothesis that chromosome accumulation on the metaphase plate promotes the separation of the associated microtubule bundles and spindle width expansion.

Figure 4

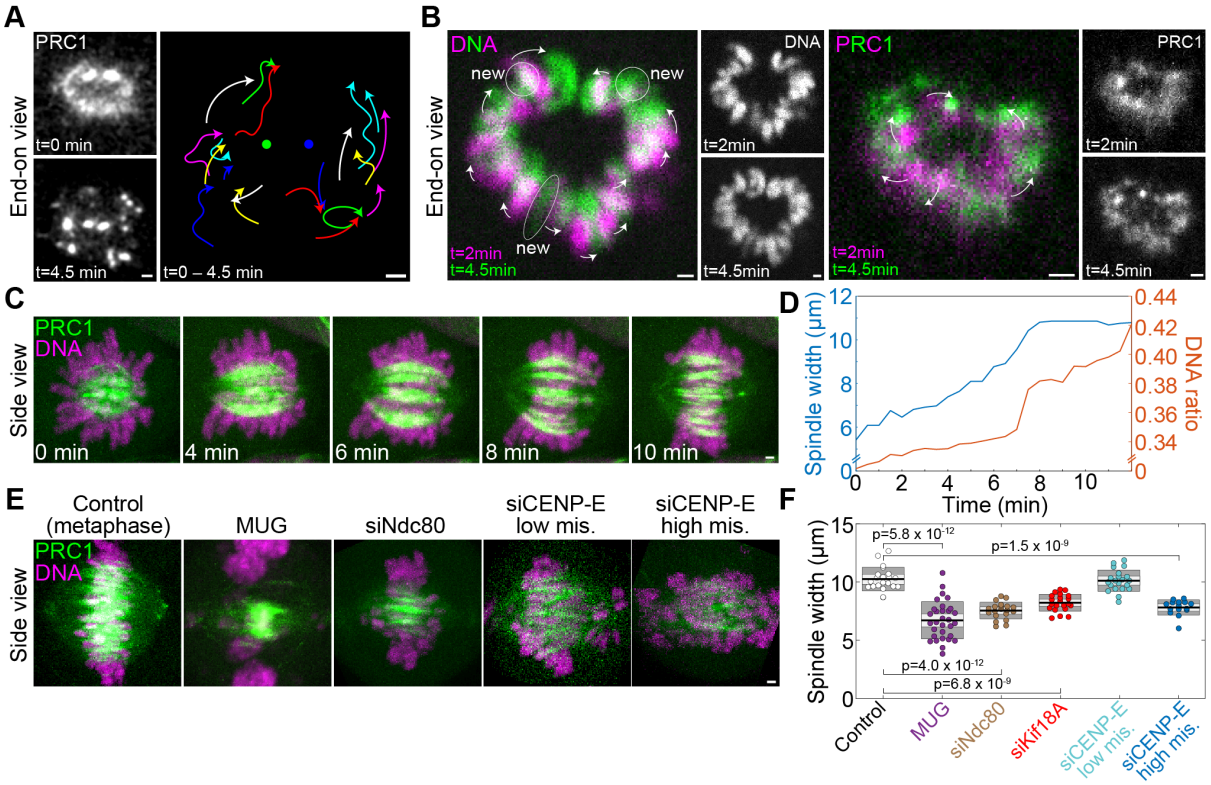

Fig. 4: Chromosomes separate microtubule bundles and increase spindle width.
a, Left, Vertical prometaphase rosette cross-section (single plane) in a HeLa-Kyoto BAC cell stably expressing PRC1-GFP, before (time 0) and after antiparallel bundle formation (4.5 minutes). Right, trajectories of all bundles from time 0 (free end of each curve) until 4.5 minutes (arrowheads), where the points between the end points were smoothed for better visibility and raw data are shown in Supplementary Video 5. Two large bundles visible at the top at time 0 are fixed in space (central points). Time interval between acquired images is 2.7 seconds. **b**, Cross-section of a vertically oriented prometaphase rosette (single plane), showing DNA stained with SiR-DNA dye (left block) or PRC1-GFP (right block), as indicated, in a HeLa-Kyoto BAC cell stably expressing PRC1-GFP, at t=2 min (magenta) and t=4.5 min (green). Individual images are shown in white at the right of the merged images. Encircled areas marked "new" denote the chromosomes that arrived to the spindle midplane between t=2 min and t=4.5 min, arrows denote the movement of DNA (left) or PRC1 bundles (right). **c**, Time-lapse images of a horizontally oriented spindle in a HeLa-Kyoto BAC cell stably expressing PRC1-GFP (green), and DNA stained with SiR-DNA (magenta) starting with early prometaphase. Sum of 41 planes is shown. **d**, Spindle width and proportion of DNA at the metaphase plate over time for the cell shown in **c**. **e**, Live-cell images of metaphase spindles in HeLa-Kyoto BAC cells stably expressing PRC1-GFP (green), and DNA stained with SiR-DNA (magenta), treated as indicated. Maximal projections of 41 planes are shown. **f**, Spindle width for the indicated treatments. The black line shows the mean; the light and dark grey areas mark 95% confidence interval on the mean and standard deviation, respectively. One-way ANOVA test showed significant difference between group means, p-values for significant differences from control are shown. Number of cells was 15-31 per group. Data for Kif18A siRNA are replotted from[77]. All scale bars, 1 μm.

Theoretical model of bundle formation

To understand the physics of bundle formation, we develop a theoretical model that allows us to identify the conditions that lead to the formation of multiple bundles, each bound to a kinetochore. We aim for a minimal model that includes key interactions between microtubules, kinetochores, chromosomes, and crosslinkers. As these interactions are complex, a minimal model is an optimal tool to understand the interplay between these multiple components and their roles in bundle formation, and to strengthen the hypotheses by comparison with experiments.

In our one-dimensional approach, representing the rim of the spindle midplane, we describe kinetochores as discrete points and explore the spatial distribution of microtubules (Fig. 5a). Kinetochores are considered as attractive points for microtubules, where multiple microtubules can bind and form a bundle. Microtubules experience mutual local attraction due to crosslinkers and inter-microtubule repulsion due to excluded volume effects. Finally, steric interactions between chromosomes and microtubules are described as a nonlocal inter-microtubule repulsion. A description of the model is given in Methods.

381 The solutions of the model show that kinetochores play an important role in the
382 formation of microtubule bundles, with peaks of microtubule density at their positions (Fig.
383 5b). These peaks increase for an increasing kinetochore-microtubule attraction, which is
384 accompanied by a decrease of the microtubule density between the kinetochores. A decrease
385 in this attraction leads to an almost homogeneous microtubule distribution. A similar behavior
386 was observed in experiments, where depletion of CENP-E led to thinner bundles and its
387 overexpression to thicker bundles (Fig. 2d and Fig. 3g,h). Thus, theory together with
388 experiments suggest that microtubules respond to the kinetochore-microtubule attraction by
389 rearranging themselves between a uniform distribution and pronounced bundles at
390 kinetochores.
391 Even though kinetochores are major attraction sites, microtubule crosslinkers also
392 affect the formation of bundles (Fig. 5c). An increase in the crosslinker concentration leads to
393 more pronounced bundles at the kinetochores, showing a similar trend as the increase in
394 kinetochore-microtubule attraction. In agreement with this theoretical result, experiments in
395 which PRC1 was overexpressed showed excessively thick overlap microtubule bundles (Fig.
396 5d and Extended Data Fig. 5). Thus, microtubule crosslinkers act cooperatively with
397 kinetochores in the formation of bundles.
398 Finally, we explored how the distance between kinetochores influences microtubule
399 distributions. When we increased the distance, the bundles at the kinetochores remained the
400 same, whereas the distribution of the microtubules between the kinetochores became
401 predominantly uniform, with more microtubules at the midpoint than for smaller inter-
402 kinetochore distance (Fig. 5e). We assume that the cases with larger and smaller distances
403 correspond to the transition of the spindle from prometaphase to metaphase, because during
404 this transition increasingly more kinetochores arrive to the spindle midplane and thus their
405 distance decreases. Indeed, we observed in experiments that in early prometaphase the
406 microtubule distribution was roughly uniform, whereas at a later phase deeper valleys between
407 the peaks appeared (Fig. 1e,f). Taken together, these results support our main hypothesis that
408 the attractive interactions due to kinetochores and crosslinkers drive the formation of
409 microtubule bundles.
410

Figure 5

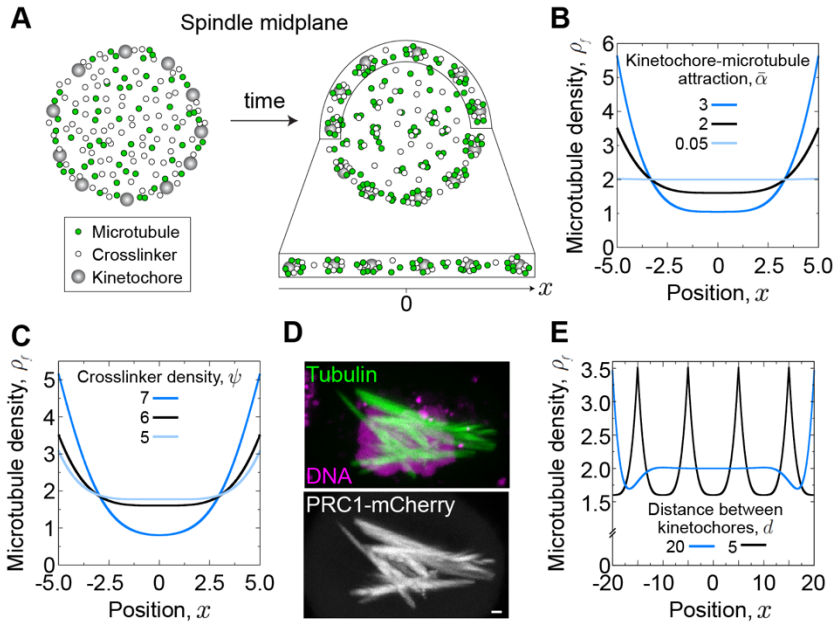

Fig. 5: Theoretical model of bundle formation.

a, Schematic representation of the model. Kinetochores (grey) are equally spaced along the edge of the spindle midplane. Microtubules (green) and crosslinkers (white) are initially uniformly distributed and gather into bundles over time. **b**, Steady-state microtubule density, ρ_f, for 3 values of the kinetochore-microtubule attraction, $\bar{\alpha}$, as indicated. Other parameters are: $\psi = 6, d = 5, \rho_b = 2, \kappa = 5$ (all parameters are dimensionless, see Methods). The kinetochores are positioned at $x = \pm d$. **c**, Steady-state microtubule density, ρ_f, for 3 values of the crosslinker density, ψ, as indicated; $\bar{\alpha} = 2, d = 5, \rho_b = 2, \kappa = 5$. **d**, Spindle in a HeLa-TDS cell with overexpressed PRC1. Top: microtubules (SiR-tubulin, green) and DNA (Hoechst 33342, magenta), bottom: PRC1-mCherry (white). Scale bar, 1 µm. **e**, Steady-state microtubule density, ρ_f, for 2 values of the distance between kinetochores, d, as indicated; $\bar{\alpha} = 2, \psi = 6, \rho_b = 2, \kappa = 5$.

Functional role of PRC1-labeled bundles in chromosome segregation fidelity

Finally, we addressed the role of overlap bundles in chromosome segregation fidelity. It has been shown that in prometaphase microtubules adjacent to the centromeres stimulate kinetochore phosphorylation and thus correction of erroneous kinetochore-microtubule attachments through microtubule binding of Borealin, a component of the Chromosome Passenger Complex[71]. We hypothesized that PRC1-bound overlap bundles are required for error correction, in a manner that Aurora B not only promotes the formation of these bundles (Fig. 2), but also uses them as tracks for the movement towards kinetochore targets to correct the wrong attachments (Fig. 6a). This hypothesis predicts that reduction of overlap

434 microtubules should lead to a decrease in outer kinetochore phosphorylation and an increase in
435 chromosome segregation errors.

436 To test these predictions, we reduced the overlap bundles by depleting PRC1, as this is
437 the most specific way to reduce these bundles known so far, which reduces overlap bundle
438 microtubules by about 50% without affecting kinetochore fibers[22]. We checked the
439 phosphorylation of serine 7 (Ser7) of CENP-A, a known Aurora B substrate[78], and found a
440 significant drop in phosphorylation after PRC1 depletion (Fig. 6b,c), which suggests that
441 PRC1-crosslinked overlap microtubules promote kinetochore phosphorylation.

442 To assess the role of overlap bundles in chromosome segregation fidelity, we first
443 analyzed lagging kinetochores in anaphase and found that PRC1 depletion caused a small
444 increase in lagging kinetochores over control cells, from 1% to 3.5% (Fig. 6d,f; see Extended
445 Data Fig. 4 for depletion efficiency)[22]. To directly examine the function of overlap bundles in
446 the correction of incorrect kinetochore attachments, we treated the cells with monastrol to block
447 the spindles in a monopolar state with high incidence of syntelic attachments, where both sister
448 kinetochores are attached to the same spindle pole[15], and washed out monastrol after 40-60
449 minutes to allow for spindle assembly (Fig. 6d). Immunofluorescence analysis of spindles in
450 anaphase showed that monastrol-treated cells that were not depleted of PRC1 had only 2.3%
451 (Fig. 6f), indicating that error correction operates in cells with proper overlap bundles. In
452 contrast, monastrol-treated cells that were depleted of PRC1 had a significantly higher
453 incidence of lagging kinetochores, 10.8% (Fig. 6e,f), revealing a role of overlap bundles in
454 error correction. Taken together, these results suggest that PRC1-bound overlap bundles have
455 a function in correcting erroneous kinetochore-microtubule attachments by promoting Aurora
456 B-driven kinetochore phosphorylation.
457

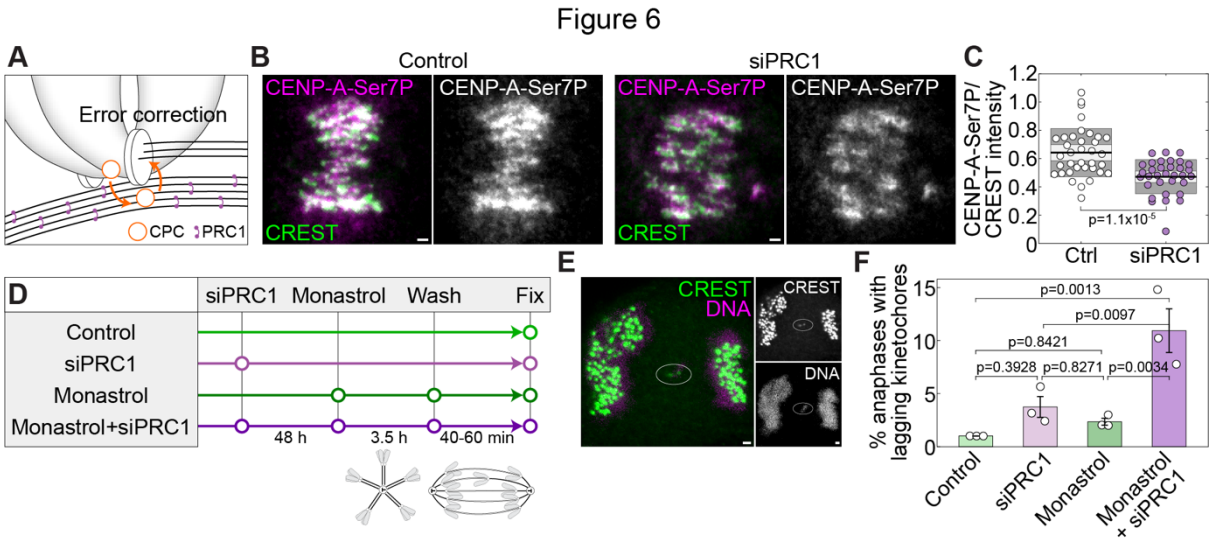

Fig. 6: PRC1-bound overlap bundles promote chromosome segregation fidelity.
a, Scheme depicting the hypothesis that antiparallel overlaps help Aurora B to reach the kinetochore components, phosphorylate them and correct erroneous attachments. **b**, Images showing anti-CENP-A-Ser7P (magenta) and CREST (green) in control (left) and PRC1-depleted HeLa cells (right), merged channels and only anti-CENP-A-Ser7P in white are shown. **c**, Ratio between anti-CENP-A-Ser7P and CREST in control (n=36) and PRC1-depleted cells (n=33), from 3 immunostaining experiments. **d**, Scheme of the protocol in which monastrol washout is used to increases erroneous attachments in prometaphase. **e**, Lagging chromosome (encircled) in anaphase in a PRC1-depleted HeLa cell after monastrol washout. Left, merged image of CREST (green) and DNA (magenta). Right, individual channels (white). **f**, Frequency of lagging kinetochores in control (3 anaphases with lagging kinetochores / 299 total anaphases), PRC1 siRNA (8/231), monastrol washout (7/298), and PRC1siRNA+monatrol washout (28/259) from 3 immunostaining experiments per condition. One-way ANOVA test showed significant difference between group means, p-values are shown. The cell line used in this figure was unlabeled HeLa-TDS. All scale bars, 1 µm.

DISCUSSION

Kinetochore- and chromosome-driven transition from a dilute microtubule array to bundles

By combining STED microscopy, a live-cell bundling assay and theory, we have shown that spindle assembly occurs through a transition in which the initially uniform microtubule array is remodeled into bundles (Fig. 7a-c). Our experiments suggest that the temporal evolution of the bundles starts with the initial dilute network of antiparallel overlaps connecting the spindle poles, which relies on augmin-mediated microtubule nucleation together with the crosslinking

485 activity of PRC1 and possibly other crosslinkers. When a kinetochore simultaneously attaches
486 to the wall of several of these microtubules via CENP-E, this promotes further bundling of
487 increasingly more microtubules by crosslinkers. While the chromosomes progressively
488 congress to the spindle equator, they crowd there and thus move together with the attached
489 bundles away from each other within the equatorial plane. As a result, the spindle cross-section
490 widens and becomes uniformly filled with bundles and the attached chromosomes, and the
491 spindle attains its metaphase shape.

492 We propose several competing mechanisms that are in action during transition to
493 bundles. There are two attractive and two repulsive effects between the microtubules.
494 Microtubules get attracted to neighboring microtubules via the crosslinkers (Fig. 7a). This
495 process is facilitated locally by kinetochores because they attach to several adjacent
496 microtubules, which brings the microtubules close to one another and promotes their bundling
497 by crosslinkers (Fig. 7a). Microtubules experience local repulsion from neighbors due to
498 excluded volume effects, and a non-local repulsion due to chromosomes whose crowding at
499 the spindle midplane moves the attached bundles away from each other (Fig. 7b). This non-
500 local repulsion helps to prevent all bundles from ending up as a single thick bundle. A bundling
501 phase transition has been studied in theoretical models of cytoskeleton networks[79,80], but here
502 we show that additional interactions such as those between microtubules and kinetochores are
503 important because they promote bundling. Yet, given that our model is one-dimensional,
504 extensions of the model that would include inter-microtubule orientation may bring about new
505 features of bundle formation.

506

507 **Kinetochores promote overlap bundle formation**

508

509 Our experiments revealed that kinetochores actively promote the formation of antiparallel
510 bundles in prometaphase. Kinetochores have been previously implicated in the formation of
511 antiparallel bundles in different contexts, for example during meiosis I in mouse oocytes, where
512 PRC1 is localized to the kinetochore through interaction with Ndc80, and facilitates bundling
513 of antiparallel overlaps in vicinity of the kinetochore[81]. As we did not find PRC1 at the
514 kinetochore in human somatic cells, the molecular mechanism of bundle formation may differ
515 in these two systems, thought the biophysical mechanisms may be similar. In anaphase in *C.*
516 *elegans* zygotes, formation of antiparallel bundles of the central spindle requires the
517 kinetochore proteins KNL-1, BUB-1, CENP-F, and CLASP[82]. CENP-E, which we identified
518 to be important for microtubule bundling in prometaphase, is also present in the central spindle

519 in anaphase, with an increased bundling activity[83,84]. Thus, it would be interesting to explore
520 the relationship between the kinetochore-related mechanisms that promote the formation of
521 microtubule bundles in prometaphase and anaphase, as well as their evolutionary aspects
522 through comparison between different organisms.

523 We found a role of CENP-E, but not of Ndc80 and dynein, in overlap bundle formation.
524 CENP-E, which is located in the fibrous corona connecting kinetochores to microtubules[67], is
525 a very long and flexible molecule with a contour length of 230 nm[85]. This may allow multiple
526 CENP-E motors at an individual kinetochore to capture and bind laterally to several nearby
527 microtubules. In contrast, Ndc80 complex and cytoplasmic dynein are only 60 and 50 nm long
528 when extended, respectively[86,87]. This difference in length may explain the importance of
529 CENP-E in microtubule bundling, even though this it is not required for lateral attachment[88].

530 Given that CENP-E interacts with PRC1[83], their interaction may also be important for
531 microtubule bundling. In addition to PRC1, other proteins that bind to antiparallel
532 microtubules, such as Eg5, likely assist bundle formation. PRC1-interacting partners Kif4A
533 and MKLP1 may also play a role, similarly to their roles in anaphase[27]. These hypotheses
534 remain to be explored in future studies.

535

536 **Chromosomes separate the bundles and determine the spindle shape**

537

538 Bundling of microtubules by crosslinkers could in principle lead to bundling of most spindle
539 microtubules into a single thick bundle. This is, however, not observed in animal spindles. In
540 contrast, yeast spindles consist of a single microtubule bundle, which is likely due to a smaller
541 number of microtubules, 40 in yeast versus 6000 in human spindles, and shorter spindles that
542 prevent microtubule bending, 1.5 μm long in yeast versus 10 μm in human cells[38,89]. We
543 propose that in animal spindles chromosomes crowding at the metaphase plate, together with
544 coupling the bundle with kinetochore during its formation, promotes bundle separation by
545 driving outward movements of the bundles, which results in spindle widening. Several lines of
546 evidence from our work support this notion. During prometaphase, as more and more
547 chromosomes arrive at the spindle midplane and fill it, the spindle gets progressively wider. In
548 agreement with this, spindles with perturbed chromosome alignment, where chromosome
549 arrangement resembles more the prometaphase state rather than metaphase, are narrower.
550 Examples studied here include depletion of Ndc80, Kif18A, and CENP-E, which have different
551 mechanistic origin of chromosome misalignment[74,75]. Thus, it is unlikely that the observed
552 spindle narrowing is due to perturbation of specific functions of these proteins, but rather due

553 to misalignment itself. Another argument comes from mitosis with unreplicated genome, in
554 which kinetochores interact with spindle microtubules but the DNA is dispersed throughout
555 the cells[10]. As expected, this resulted in narrow spindles, but fully formed bundles due to the
556 presence of kinetochores.
557 Previous work has shown that in HeLa cells, which have a variable number of
558 chromosomes[90], spindle width increases with the number of chromosomes[53]. This result also
559 supports the chromosome crowding hypothesis. Finally, a striking example comes from the
560 finding that a single microtubule bundle connects the spindle poles with chromosomes lying
561 along the sides upon expression of a kinase-inactive Aurora B[91], in agreement with our
562 hypothesis.
563
564 **PRC1-linked overlap microtubules promote chromosome segregation fidelity**
565
566 We have shown that PRC1-bound overlap bundles are required for the correction of synthelic
567 kinetochore-microtubule attachments after spindle assembly from a monopole state. PRC1
568 depletion, which reduces the number of microtubules in the overalp bundles, resulted not only
569 in an increase in lagging kinetochores, but also in decreased kinetochore phosphorylation. By
570 combing these results with a previous work showing that Borealin binding to microtubules
571 stimulates kinetochore phosphorylation and correction of erroneous kinetochore-microtubule
572 attachments[71], we propose that Aurora B, being part of the Chromosome Passenger Complex
573 together with Borealin, not only promotes the formation of PRC1-linked overlap bundles, but
574 also uses them as tracks for the movement towards kinetochores to correct the wrong
575 attachments. The molecular details of this PRC1-based error-correction mechanism remain an
576 exciting topic for future studies.
577 In conclusion, our results reveal that a transition of microtubules from a loose array to
578 bundles, dependent on kinetochores that serve as attraction sites and chromosomes that provide
579 repulsion, promotes spindle assembly. In a broader sense, our study reveals general principles
580 of organization of cytoskeletal filaments. The concepts of attraction sites as drivers of bundle
581 formation may be relevant in other contexts, for example in the formation of actin bundles,
582 where adherens junctions and focal adhesions may act as such sites. Overall, we expect that
583 mechanisms similar to the ones identified here, though with different molecular players, act in
584 a variety of cytoskeletal systems to generate specific filament arrangements required for their
585 function.
586

Figure 7

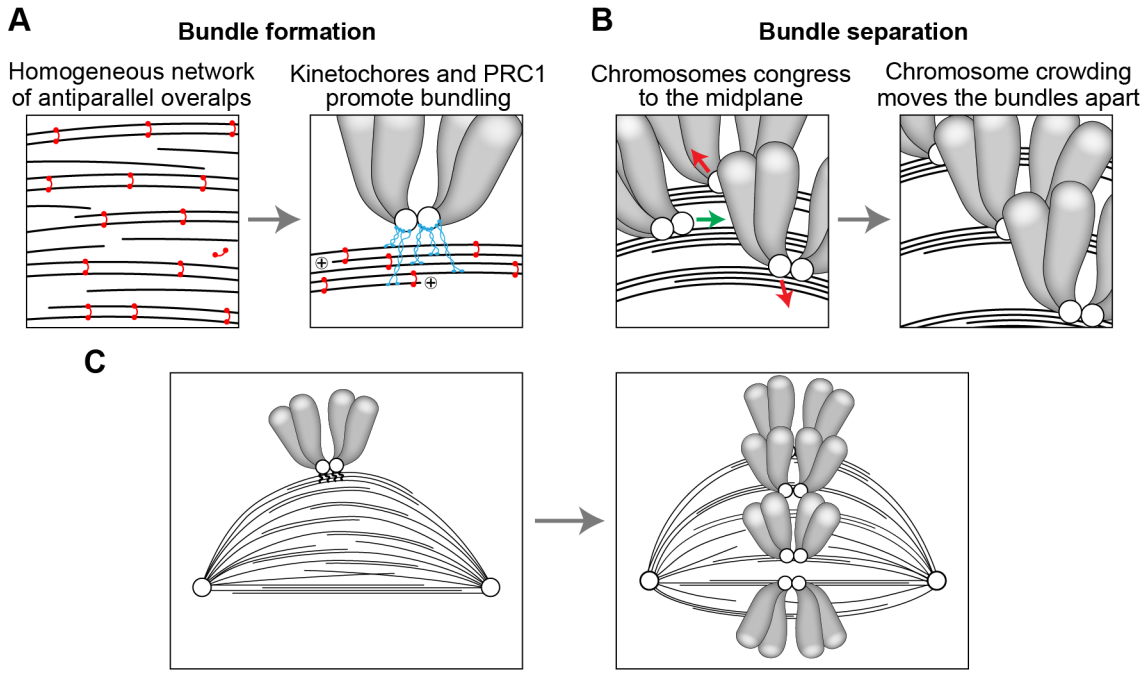

Fig. 7: Model for kinetochore driven overlap formation.

a, A loose microtubule network consisting of uniformly distributed antiparallel overlaps linked by PRC1 (red) undergoes a transition to tight bundles due to the microtubule-binding activity of kinetochores (CENP-E, blue). **b**, Bundles are separated (red arrows) during chromosome congression (green arrow) to the spindle midplane and steric effects of neighboring chromosome arms. **c**, The processes depicted in **a** and **b** lead to a transition from the prometaphase rosette (left), with a loose network of microtubules and laterally attached chromosomes, to a more mature spindle in late prometaphase (right), with distinct and separated bundles.

598 **REFERENCES**
599

600 1. Prosser, S. L. & Pelletier, L. Mitotic spindle assembly in animal cells: A fine balancing
601 act. *Nat. Rev. Mol. Cell Biol.* **18**, 187–201 (2017).
602 2. McIntosh, J. R., Molodtsov, M. I. & Ataullakhanov, F. I. Biophysics of mitosis. *Q.*
603 *Rev. Biophys.* **45**, 147–207 (2012).
604 3. Pavin, N. & Tolić, I. M. Self-Organization and Forces in the Mitotic Spindle. *Annu.*
605 *Rev. Biophys.* **45**, 279–298 (2016).
606 4. McDonald, K. L., O'Toole, E. T., Mastronarde, D. N. & McIntosh, J. R. Kinetochore
607 microtubules in PTK cells. *J. Cell Biol.* **118**, 369–383 (1992).
608 5. Cheeseman, I. M. & Desai, A. Molecular architecture of the kinetochore-microtubule
609 interface. *Nat. Rev. Mol. Cell Biol.* **9**, 33–46 (2008).
610 6. Mastronarde, D. N., McDonald, K. L., Ding, R. & McIntosh, J. R. Interpolar spindle
611 microtubules in PTK cells. *J. Cell Biol.* **123**, 1475–1489 (1993).
612 7. Mitchison, T. J. & Kirschner, M. W. Properties of the Kinetochore In Vitro. I.
613 Microtubule nucleation and tubulin binding. *J. Cell Biol.* **101**, 755–765 (1985).
614 8. Rieder, C. L. & Alexander, S. P. Kinetochores are transported poleward along a single
615 astral microtubule during chromosome attachment to the spindle in newt lung cells. *J.*
616 *Cell Biol.* **110**, 81–95 (1990).
617 9. Wollman, R. *et al.* Efficient chromosome capture requires a bias in the 'search-and-
618 capture' process during mitotic-spindle assembly. *Curr. Biol.* **15**, 828–832 (2005).
619 10. O'Connell, C. B., Lončarek, J., Kaláb, P. & Khodjakov, A. Relative contributions of
620 chromatin and kinetochores to mitotic spindle assembly. *J. Cell Biol.* **187**, 43–51
621 (2009).
622 11. Sikirzhytski, V. *et al.* Microtubules assemble near most kinetochores during early
623 prometaphase in human cells. *J. Cell Biol.* **217**, 2647–2659 (2018).
624 12. Renda, F. *et al.* Non-centrosomal microtubules at kinetochores promote rapid
625 chromosome biorientation during mitosis in human cells. *Curr. Biol.* **in press**, (2022).
626 13. Sawin, K. E., Leguellec, K., Philippe, M. & Mitchison, T. J. Mitotic spindle
627 organization by a plus-end-directed microtubule motor. *Nature* **359**, 540–543 (1992).
628 14. Kapitein, L. C. *et al.* The bipolar mitotic kinesin Eg5 moves on both microtubules that
629 it crosslinks. *Nature* **435**, (2005).
630 15. Kapoor, T. M., Mayer, T. U., Coughlin, M. L. & Mitchison, T. J. Probing spindle
631 assembly mechanisms with monastrol, a small molecule inhibitor of the mitotic
632 kinesin, Eg5. *J. Cell Biol.* **150**, (2000).
633 16. Blangy, A. *et al.* Phosphorylation by p34cdc2 regulates spindle association of human
634 Eg5, a kinesin-related motor essential for bipolar spindle formation in vivo. *Cell* **83**,
635 1159–1169 (1995).
636 17. Kajtez, J. *et al.* Overlap microtubules link sister k-fibres and balance the forces on bi-
637 oriented kinetochores. *Nat. Commun.* **7**, (2016).
638 18. Milas, A. & Tolić, I. Relaxation of interkinetochore tension after severing of a k-fiber
639 depends on the length of the k-fiber stub. *Matters Sel.* (2016)
640 doi:10.19185/matters.201603000025.
641 19. Elting, M. W., Prakash, M., Udy, D. B. & Dumont, S. Mapping Load-Bearing in the
642 Mammalian Spindle Reveals Local Kinetochore Fiber Anchorage that Provides
643 Mechanical Isolation and Redundancy. *Curr. Biol.* **27**, 2112-2122.e5 (2017).
644 20. Maiato, H., Gomes, A. M., Sousa, F. & Barisic, M. Mechanisms of chromosome
645 congression during mitosis. *Biology (Basel).* **6**, 1–56 (2017).
646 21. Suresh, P., Long, A. F. & Dumont, S. Microneedle manipulation of the mammalian
647 spindle reveals specialized, short-lived reinforcement near chromosomes. *Elife* **9**, 1–22

(2020).
22. Jagrić, M., Risteski, P., Martinčić, J., Milas, A. & Tolić, I. M. Optogenetic control of prc1 reveals its role in chromosome alignment on the spindle by overlap length-dependent forces. *Elife* **10**, 1–79 (2021).
23. Risteski, P. *et al.* Coordinated poleward flux of sister kinetochore fibers drives chromosome alignment. *bioRxiv* 2020.12.30.424837 (2021) doi:10.1101/2020.12.30.424837.
24. Brust-Mascher, I., Civelekoglu-Scholey, G., Kwon, M., Mogilner, A. & Scholey, J. M. Model for anaphase B: Role of three mitotic motors in a switch from poleward flux to spindle elongation. *Proc. Natl. Acad. Sci. U. S. A.* **101**, 15938–15943 (2004).
25. Brust-Mascher, I., Sommi, P., Cheerambathur, D. K. & Scholey, J. M. Kinesin-5–dependent Poleward Flux and Spindle Length Control in Drosophila Embryo Mitosis. *Mol. Biol. Cell* **20**, 1749–1762 (2009).
26. Vukušić, K. *et al.* Microtubule Sliding within the Bridging Fiber Pushes Kinetochore Fibers Apart to Segregate Chromosomes. *Dev. Cell* **43**, 11-23.e6 (2017).
27. Vukušić, K., Ponjavić, I., Buđa, R., Risteski, P. & Tolić, I. M. Microtubule-sliding modules based on kinesins EG5 and PRC1-dependent KIF4A drive human spindle elongation. *Dev. Cell* **56**, 1253-1267.e10 (2021).
28. Yu, C. H. *et al.* Central-spindle microtubules are strongly coupled to chromosomes during both anaphase A and anaphase B. *Mol. Biol. Cell* **30**, 2503–2514 (2019).
29. Asthana, J., Cade, N. I., Normanno, D., Lim, W. M. & Surrey, T. Gradual compaction of the central spindle decreases its dynamicity in PRC1 and EB1 gene-edited cells. *Life Sci. Alliance* **4**, (2021).
30. Janson, M. E. *et al.* Crosslinkers and Motors Organize Dynamic Microtubules to Form Stable Bipolar Arrays in Fission Yeast. *Cell* **128**, 357–368 (2007).
31. Kapitein, L. C. *et al.* Microtubule-Driven Multimerization Recruits ase1p onto Overlapping Microtubules. *Curr. Biol.* **18**, 1713–1717 (2008).
32. Subramanian, R. *et al.* Insights into antiparallel microtubule crosslinking by PRC1, a conserved nonmotor microtubule binding protein. *Cell* **142**, 433–443 (2010).
33. Bieling, P., Telley, I. A. & Surrey, T. A minimal midzone protein module controls formation and length of antiparallel microtubule overlaps. *Cell* **142**, 420–432 (2010).
34. Edelmaier, C. J. *et al.* Mechanisms of chromosome biorientation and bipolar spindle assembly analyzed by computational modeling. *Elife* **9**, (2020).
35. Blackwell, R. *et al.* Physical determinants of bipolar mitotic spindle assembly and stability in fission yeast. *Sci. Adv.* **3**, (2017).
36. Winters, L. *et al.* Pivoting of microtubules driven by minus-end-directed motors leads to spindle assembly. *BMC Biol.* **17**, (2019).
37. Nédélec, F. Computer simulations reveal motor properties generating stable antiparallel microtubule interactions. *J. Cell Biol.* **158**, (2002).
38. Kiewisz, R., Fabig, G., Conway, W., Needleman, D. & Müller-Reichert, T. Three-dimensional structure of the kinetochore-fibers in human mitotic spindles. *bioRxiv* 2021.11.13.468347 (2021).
39. Needleman, D. & Dogic, Z. Active matter at the interface between materials science and cell biology. *Nat. Rev. Mater.* **2**, 17048 (2017).
40. Roostalu, J., Rickman, J., Thomas, C., Nédélec, F. & Surrey, T. Determinants of Polar versus Nematic Organization in Networks of Dynamic Microtubules and Mitotic Motors. *Cell* **175**, (2018).
41. Wu, K. T. *et al.* Transition from turbulent to coherent flows in confined three-dimensional active fluids. *Science* **355**, (2017).
42. Hitt, A. L., Cross, A. R. & Williams, R. C. Microtubule solutions display nematic

liquid crystalline structure. *J. Biol. Chem.* **265**, 1639–1647 (1990).
43. Kierfeld, J., Kühne, T. & Lipowsky, R. Discontinuous unbinding transitions of filament bundles. *Phys. Rev. Lett.* **95**, 1–4 (2005).
44. Huisman, B. A. H., Bolhuis, P. G. & Fasolino, A. Phase transition to bundles of flexible supramolecular polymers. *Phys. Rev. Lett.* **100**, (2008).
45. Borukhov, I., Bruinsma, R. F., Gelbart, W. M. & Liu, A. J. Structural polymorphism of the cytoskeleton: A model of linker-assisted filament aggregation. *Proc. Natl. Acad. Sci. U. S. A.* **102**, (2005).
46. Kachan, D., Müller, K. W., Wall, W. A. & Levine, A. J. Discontinuous bundling transition in semiflexible polymer networks induced by Casimir interactions. *Phys. Rev. E* **94**, (2016).
47. Maxian, O., Donev, A. & Mogilner, A. Interplay between Brownian motion and cross-linking kinetics controls bundling dynamics in actin networks. *bioRxiv* 2021.09.17.460819 (2021) doi:https://doi.org/10.1101/2021.09.17.460819.
48. Huang, B., Babcock, H. & Zhuang, X. Breaking the diffraction barrier: Super-resolution imaging of cells. *Cell* **143**, 1047–1058 (2010).
49. Bolzer, A. *et al.* Three-dimensional maps of all chromosomes in human male fibroblast nuclei and prometaphase rosettes. *PLoS Biol.* **3**, 0826–0842 (2005).
50. Itoh, G. *et al.* Lateral attachment of kinetochores to microtubules is enriched in prometaphase rosette and facilitates chromosome alignment and bi-orientation establishment. *Sci. Rep.* **8**, 1–18 (2018).
51. Goshima, G., Mayer, M., Zhang, N., Stuurman, N. & Vale, R. D. Augmin: A protein complex required for centrosome-independent microtubule generation within the spindle. *J. Cell Biol.* **181**, 421–429 (2008).
52. Uehara, R. *et al.* The augmin complex plays a critical role in spindle microtubule generation for mitotic progression and cytokinesis in human cells. *Proc. Natl. Acad. Sci. U. S. A.* **106**, 6998–7003 (2009).
53. Polak, B., Risteski, P., Lesjak, S. & Tolić, I. M. PRC 1-labeled microtubule bundles and kinetochore pairs show one-to-one association in metaphase. *EMBO Rep.* **18**, 217–230 (2017).
54. O'Toole, E., Morphew, M. & Richard McIntosh, J. Electron tomography reveals aspects of spindle structure important for mechanical stability at metaphase. *Mol. Biol. Cell* **31**, 184–195 (2020).
55. Nagele, R., Freeman, T., Mcmorrow, L. & Lee, H. Precise spatial positioning of chromosomes during prometaphase: evidence for chromosomal order. *Science* **270**, 1831–1835 (1995).
56. Chaly, N. & Brown, D. L. The prometaphase configuration and chromosome order in early mitosis. *J. Cell Sci.* **91**, 325–335 (1988).
57. DeLuca, J. G. *et al.* Kinetochore Microtubule Dynamics and Attachment Stability Are Regulated by Hec1. *Cell* **127**, 969–982 (2006).
58. Welburn, J. P. I. *et al.* Aurora B Phosphorylates Spatially Distinct Targets to Differentially Regulate the Kinetochore-Microtubule Interface. *Mol. Cell* **38**, 383–392 (2010).
59. Shrestha, R. L. *et al.* Aurora-B kinase pathway controls the lateral to end-on conversion of kinetochore-microtubule attachments in human cells. *Nat. Commun.* **8**, 1–12 (2017).
60. Mortlock, A. A. *et al.* Discovery, synthesis, and in vivo activity of a new class of pyrazoloquinazolines as selective inhibitors of aurora B kinase. *J. Med. Chem.* **50**, 2213–2224 (2007).
61. Dennis, M. *et al.* Phase i study of the Aurora B kinase inhibitor barasertib (AZD1152)

748 to assess the pharmacokinetics, metabolism and excretion in patients with acute
749 myeloid leukemia. *Cancer Chemother. Pharmacol.* **70**, 461–469 (2012).
750 62. Liu, D., Vader, G., Vromans, M. J. M., Lampson, M. A. & Lens, S. M. A. Sensing
751 chromosome bi-orientation by spatial separation of Aurora B kinase from kinetochore
752 substrates. *Science* **323**, 1350–1353 (2009).
753 63. Kallio, M. J., McCleland, M. L., Todd Stukenberg, P. & Gorbsky, G. J. Inhibition of
754 Aurora B kinase blocks chromosome segregation, overrides the spindle checkpoint,
755 and perturbs microtubule dynamics in mitosis. *Curr. Biol.* **12**, 900–905 (2002).
756 64. Wang, E., Ballister, E. R. & Lampson, M. A. Aurora B dynamics at centromeres create
757 a diffusion-based phosphorylation gradient. *J. Cell Biol.* **194**, 539–549 (2011).
758 65. Kim, Y., Holland, A. J., Lan, W. & Cleveland, D. W. Aurora kinases and protein
759 phosphatase 1 mediate chromosome congression through regulation of CENP-E. *Cell*
760 **142**, 444–455 (2010).
761 66. Cheeseman, I. M., Chappie, J. S., Wilson-Kubalek, E. M. & Desai, A. The Conserved
762 KMN Network Constitutes the Core Microtubule-Binding Site of the Kinetochore.
763 *Cell* **127**, 983–997 (2006).
764 67. Yao, X., Anderson, K. L. & Cleveland, D. W. The microtubule-dependent motor
765 centromere-associated protein E (CENP- E) is an integral component of kinetochore
766 corona fibers that link centromeres to spindle microtubules. *J. Cell Biol.* **139**, 435–447
767 (1997).
768 68. Qian, X. *et al.* Discovery of the first potent and selective inhibitor of centromere-
769 associated protein E: GSK923295. *ACS Med. Chem. Lett.* **1**, 30–34 (2010).
770 69. Griffis, E. R., Stuurman, N. & Vale, R. D. Spindly, a novel protein essential for
771 silencing the spindle assembly checkpoint, recruits dynein to the kinetochore. *J. Cell*
772 *Biol.* **177**, 1005–1015 (2007).
773 70. Ciferri, C. *et al.* Implications for Kinetochore-Microtubule Attachment from the
774 Structure of an Engineered Ndc80 Complex. *Cell* **133**, 427–439 (2008).
775 71. Trivedi, P. *et al.* The binding of Borealin to microtubules underlies a tension
776 independent kinetochore-microtubule error correction pathway. *Nat. Commun.* **10**,
777 (2019).
778 72. Wise, D. A. & Brinkley, B. R. Mitosis in cells with unreplicated genomes (MUGs):
779 Spindle assembly and behavior of centromere fragments. *Cell Motil. Cytoskeleton* **36**,
780 (1997).
781 73. Martin-Lluesma, S., Stucke, V. M. & Nigg, E. A. Role of Hec1 in spindle checkpoint
782 signaling and kinetochore recruitment of Mad1/Mad2. *Science* **297**, 2267–2270 (2002).
783 74. DeLuca, J. G., Moree, B., Hickey, J. M., Kilmartin, J. V. & Salmon, E. D. hNuf2
784 inhibition blocks stable kinetochore-microtubule attachment and induces mitotic cell
785 death in HeLa cells. *J. Cell Biol.* **159**, (2002).
786 75. Stumpff, J., von Dassow, G., Wagenbach, M., Asbury, C. & Wordeman, L. The
787 Kinesin-8 Motor Kif18A Suppresses Kinetochore Movements to Control Mitotic
788 Chromosome Alignment. *Dev. Cell* **14**, 252–262 (2008).
789 76. Mayr, M. I. *et al.* The Human Kinesin Kif18A Is a Motile Microtubule Depolymerase
790 Essential for Chromosome Congression. *Curr. Biol.* **17**, (2007).
791 77. Trupinić, M. *et al.* Twist of the mitotic spindle culminates at anaphase onset and
792 depends on microtubule-associated proteins along with external forces. *bioRxiv* (2020)
793 doi:10.1101/2020.12.27.424486.
794 78. Zeitlin, S. G., Shelby, R. D. & Sullivan, K. F. CENP-A is phosphorylated by Aurora B
795 kinase and plays an unexpected role in completion of cytokinesis. *J. Cell Biol.* **155**,
796 1147–1157 (2001).
797 79. Chandrasekaran, A., Upadhyaya, A. & Papoian, G. A. Remarkable structural

transformations of actin bundles are driven by their initial polarity, motor activity, crosslinking, and filament treadmilling. *PLoS Comput. Biol.* **15**, (2019).
80. Weirich, K. L. *et al.* Liquid behavior of cross-linked actin bundles. *Proc. Natl. Acad. Sci. U. S. A.* **114**, 2131–2136 (2017).
81. Yoshida, S. *et al.* Prc1-rich kinetochores are required for error-free acentrosomal spindle bipolarization during meiosis I in mouse oocytes. *Nat. Commun.* **11**, (2020).
82. Maton, G. *et al.* Kinetochore components are required for central spindle assembly. *Nat. Cell Biol.* **17**, 697–705 (2015).
83. Liu, X. *et al.* Mitotic motor CENP-E cooperates with PRC1 in temporal control of central spindle assembly. *J. Mol. Cell Biol.* **12**, 654–665 (2020).
84. Vitre, B. *et al.* Kinetochore-microtubule attachment throughout mitosis potentiated by the elongated stalk of the kinetochore kinesin CENP-E. *Mol. Biol. Cell* **25**, 2272–2281 (2014).
85. Kim, Y., Heuser, J. E., Waterman, C. M. & Cleveland, D. W. CENP-E combines a slow, processive motor and a flexible coiled coil to produce an essential motile kinetochore tether. *J. Cell Biol.* **181**, 411–419 (2008).
86. Wei, R. R., Sorger, P. K. & Harrison, S. C. Molecular organization of the Ndc80 complex, an essential kinetochore component. *Proc. Natl. Acad. Sci. U. S. A.* **102**, 5363–5367 (2005).
87. Vallee, R. B., Wall, J. S., Paschal, B. M. & Shpetner, H. S. Microtubule-associated protein 1c from brain is a two-headed cytosolic dynein. *Nature* **332**, 561–563 (1988).
88. Shrestha, R. L. & Draviam, V. M. Lateral to end-on conversion of chromosome-microtubule attachment requires kinesins cenp-e and MCAK. *Curr. Biol.* **23**, 1514–1526 (2013).
89. Winey, M. *et al.* Three-dimensional ultrastructural analysis of the Saccharomyces cerevisiae mitotic spindle. *J. Cell Biol.* **129**, 1601–1615 (1995).
90. Landry, J. J. M. *et al.* The genomic and transcriptomic landscape of a hela cell line. *G3 Genes, Genomes, Genet.* **3**, 1213–1224 (2013).
91. Murata-Hori, M. & Wang, Y. L. The kinase activity of aurora B is required for kinetochore-microtubule interactions during mitosis. *Curr. Biol.* **12**, (2002).
92. Yang, J. *et al.* AZD1152, a novel and selective aurora B kinase inhibitor, induces growth arrest, apoptosis, and sensitization for tubulin depolymerizing agent or topoisomerase II inhibitor in human acute leukemia cells in vitro and in vivo. *Blood* **110**, (2007).
93. Wood, K. W. *et al.* Antitumor activity of an allosteric inhibitor of centromere-associated protein-E. *Proc. Natl. Acad. Sci. U. S. A.* **107**, 5839–5844 (2010).
94. Bennett, A. *et al.* Cenp-E inhibitor GSK923295: Novel synthetic route and use as a tool to generate aneuploidy. *Oncotarget* **6**, 20921–20932 (2015).
95. Rizk, A. *et al.* Segmentation and quantification of subcellular structures in fluorescence microscopy images using Squassh. *Nat. Protoc.* **9**, 586–596 (2014).

840 **METHODS**

841

842 **Cell lines and culture**

843 Experiments were carried out using unlabeled human HeLa-TDS cells (also referred to as
844 untransfected HeLa cells) from the High-Throughput Technology Development Studio (Max
845 Planck Institute of Molecular Cell Biology and Genetics, Dresden, Germany), HeLa-Kyoto
846 BAC lines stably expressing PRC1-GFP (also referred to as HeLa PRC1-GFP cells) are
847 courtesy of Ina Poser and Tony Hyman (Max Planck Institute of Molecular Cell Biology and
848 Genetics, Dresden, Germany), and human hTERT-RPE1 (hTERT-immortalized retinal
849 pigment epithelium) cells stably expressing CENP-A-GFP and Centrin1-GFP, courtesy of
850 Alexey Khodjakov (Wadsworth Center, New York State Department of Health, Albany, NY,
851 USA). All cell lines were cultured in flasks in Dulbecco's Modified Eagle's Medium with 1 g/L
852 D-glucose, pyruvate and L-glutamine (DMEM, Lonza, Basel, Switzerland), supplemented with
853 10% (vol/vol) heat-inactivated Fetal Bovine Serum (FBS, Sigma Aldrich, St. Louis, MO, USA)
854 and penicillin (100 IU/mL)/streptomycin (100 mg/mL) solution (Lonza, Basel, Switzerland).
855 For the selection of HeLa PRC1-GFP cell lines, 50 µg/ml geneticin was added to the medium
856 (Life Technologies, Waltham, MA, USA). The cells were kept at 37°C and 5% CO_2 in a
857 humidified incubator (Galaxy 170S CO_2, Eppendorf, Hamburg, Germany) and regularly
858 passaged at the confluence of 70-80%.

859

860 **Sample preparation, siRNA, plasmids, and dyes**

861 At 80% confluence, DMEM medium was removed from the flask and cells were washed with
862 5 ml of phosphate buffered saline (PBS). Then, 1 ml 1% trypsin/ethylenediaminetetraacetic
863 acid (EDTA, Biochrom AG, Berlin, Germany) was added to the flask and cells were incubated
864 at 37°C and 5% CO_2 in a humidified incubator for 5 minutes. After the incubation, trypsin was
865 blocked by adding 2 ml of DMEM medium. For RNAi experiments, the cells were seeded to
866 reach 60% confluence the next day and cultured on 35 mm uncoated dishes with 0.17 mm (#1.5
867 coverglass) glass thickness (MatTek Corporation, Ashland, MA, USA) in 2 mL DMEM
868 medium with the supplements described above. After one day of growth, cells were transfected
869 with either targeting or non-targeting siRNA constructs which were diluted in OPTI-MEM
870 medium (Life Technologies, Waltham, MA, USA) to a final concentration of 100 nM in the
871 medium with cells. All transfections were performed 48 hours prior to imaging using
872 Lipofectamine RNAiMAX Reagent (Life Technologies, Waltham, MA, USA) according to the
873 instructions provided by the manufacturer. After four hours of treatment, the medium was

874 changed to the DMEM medium. The constructs used were human HAUS6 siRNA (L-018372-
875 01-0005, Dharmacon, Lafayette, CO, USA), human ON-TARGET plus SMART pool CENP-
876 E siRNA (L-003252-00-0010, Dharmacon, Lafayette, CO, USA), ON-TARGET human
877 CCDC99 siRNA (L-016970-00-0010, Dharmacon, Lafayette, CO, USA), human Ndc80
878 siRNA (HA12977117-004; Merck, Darmstadt, Germany), human ON-TARGET PRC1 siRNA
879 (L-019491-00-0020, Dharmacon) and control siRNA (D-001810-10-05, Dharmacon,
880 Lafayette, CO, USA).
881 For experiments with CENP-B-INCENP-GFP, unlabeled HeLa-TDS cells were
882 transfected with CENP-B-INCENP-GFP (Addgene, plasmid #45238), and for live-cell
883 imaging also with mCherry-PRC1 plasmid provided by Casper C. Hoogenraad (Utrecht
884 University, Utrecht, The Netherlands). 1×10^6 cells were transfected using Lipofectamine 3000
885 Reagent (L3000001, Life Technologies, Waltham, MA, US) with 1.5 µg of plasmid DNA for
886 both plasmids. For CENP-E overexpression experiments, unlabeled HeLa-TDS cells were
887 transfected with 2 µg of CENP-E-GFP plasmid (gift from Marin Barišić, Danish Cancer
888 Society Research Center, Copenhagen, Denmark). To overexpress PRC1, unlabeled HeLa-
889 TDS cells were transfected with 5 µg of mCherry-PRC1 plasmid. Transfection of both
890 unlabeled HeLa-TDS and HeLa PRC1-GFP cells was performed 25–35 h before imaging.
891 In order to visualize microtubules, human hTERT-RPE1 cells stably expressing CENP-
892 A-GFP and Centrin1-GFP and unlabeled HeLa-TDS cells were stained to a final concentration
893 of 100 nM with a far-red silicon rhodamine (SiR)-tubulin-670 dye (Spirochrome, Stein am
894 Rhein, Switzerland), 45 minutes to 2 hours prior to imaging. In order to avoid dye efflux, a
895 broad-spectrum efflux pump inhibitor verapamil (Spirochrome, Stein am Rhein, Switzerland)
896 was added at a final concentration of 0.5 µM to the cells along with SiR-tubulin. For
897 chromosome visualization, HeLa PRC1-GFP cells were stained with 100 nM SiR-DNA dye
898 for 20 minutes to 2 hours prior to imaging. To identify the cells in mitosis by condensed
899 chromosomes in the PRC1 overexpression experiment on unlabeled HeLa-TDS cells, 50 µL of
900 NucBlue Live Ready Probes Reagent (Hoechst 33342, Invitrogen by Thermo Fisher Scientific,
901 Waltham, MA, USA) was added to the dishes 1 min before imaging.
902
903 **Drug treatments**
904 The stock solution of the Aurora B kinase inhibitor Barasertib (AZD1152-HQPA,
905 Selleckchem, Munich, Germany) was prepared in Dimethyl sulfoxide (DMSO) to a final
906 concentration of 1 mM. The working solution was prepared in DMEM at 600 nM and at the
907 time of treatment, the working solution was added to cells at 1:1 volume ratio to obtain a final

908 concentration of 300 nM; IC50 is 0.35 nM for this compound[92]. Barasertib was added at early
909 prometaphase rosette in HeLa PRC1-GFP cell line. Appearance of predominantly
910 prometaphase-like spindles[63] in the sample imaged 1 hour post-treatment confirmed the effect
911 of Barasertib on Aurora B.
912 The stock solution of the CENP-E inhibitor GSK-923295 (MedChemExpress,
913 Monmouth Junction, NJ, USA) was prepared in DMSO at a final concentration of 8 mM. The
914 working solution was prepared in DMEM at 200 nM. At the time of treatment, the working
915 solution was added to cells at 1:1 volume ratio to obtain a final concentration of 100 nM; IC50
916 value of compound is 3.2 nM[93]. GSK-923295 was added at early prometaphase rosette in HeLa
917 PRC1-GFP cell line immediately before the start of imaging, and 2 hours before imaging in
918 hTERT-RPE1 cell line expressing CenpA-GFP and Centrin1-GFP. Appearance of spindles
919 blocked in prometaphase with a fraction of kinetochores trapped around polar region of the
920 spindle at 30 minutes post-treatment[94] confirmed the effect of GSK-923295. For hTERT-RPE1
921 cells, mock treatment was the same concentration of DMSO that was used for preparation of
922 the inhibitors.
923 Nocodazole (HY-13520, MedChemExpress, Monmouth Junction, NJ, USA) working
924 solution was prepared in DMEM at 2 μM. At the time of treatment, the working solution was
925 added to cells at 1:1 volume ratio to obtain a final concentration of 1 μM. Nocodazole was
926 added at early prometaphase rosette in HeLa PRC1-GFP cell line immediately before the start
927 of imaging.
928 Monastrol (HY-101071A/CS-6183, MedChemExpress, Monmouth Junction, NJ, USA)
929 working solution (100 μM) was added in the dish with untransfected HeLa cells at a final
930 concentration of 100 nM.
931
932 **Inducing mitosis with unreplicated genome (MUG)**
933 MUG is induced by incubation of cells in hydroxyurea and caffeine[72], a gift from Anđela
934 Horvat and Neda Slade (Laboratory for protein dynamics, Ruđer Bošković Institute, Zagreb,
935 Croatia). The stock solutions of hydroxyurea and caffeine were prepared at a concentration of
936 175 mM and 200 mM, respectively. The stock solution was diluted in DMEM to the final
937 concentration of 2 mM for hydroxyurea and 5 mM for caffeine. The amount of $1x10^5$ HeLa
938 PRC1-GFP cells were counted using the Improved Neubauer chamber (BRAND GMBH + CO
939 KG, Wertheim, Germany), seeded and cultured in 2 ml DMEM at 37°C and 5% CO_2 on 35 mm
940 glass coverslip uncoated dishes with 0.17 mm (#1.5 coverglass) glass thickness (MatTek
941 Corporation, Ashland, MA, USA). After 12 hours, the medium was replaced with 2 mL DMEM

942 containing 2 mM hydroxyurea and incubated for 20 hours at 37°C and 5% CO_2. After 20 hours,
943 the medium was again replaced with a medium containing 2 mM hydroxyurea and 5 mM
944 caffeine and the cells were again incubated at 37°C and 5% CO_2. The cells were imaged 18
945 hours later.
946
947 **Immunocytochemistry**
948 HeLa cells expressing PRC1-GFP and untransfected HeLa cells were grown on glass-bottom
949 dishes (14 mm, No. 1.5, MatTek Corporation, Darmstadt, Germany) and fixed by 1 ml of ice-
950 cold methanol for 1 min at -20°C. Following fixation, cells were washed 3 times for 5 minutes
951 with 1 ml of PBS and permeabilized with 0.5% Triton-X-100 in water for 15 minutes at room
952 temperature. To block unspecific binding, cells were incubated in 1 ml of blocking buffer (1%
953 normal goat serum, NGS) for 1 hour at room temperature. Cells were then washed 3 times for
954 5 minutes with 1 ml of PBS and incubated with 500 µl of primary antibody solution overnight
955 at 4°C. The following primary antibodies were used: mouse monoclonal PRC1 (sc-376983,
956 Santa Cruz Biotechnology), diluted 1:100, rat anti-alpha-tubulin YL1/2 (MA1-80017,
957 Invitrogen, CA, SAD), diluted 1:500, mouse IgG monoclonal anti-GFP (Ref 11814460001,
958 LOT42903200, Roche), diluted 1:100, rabbit anti-alpha-tubulin (SAB4500087, LOT 310379,
959 Sigma Aldrich), diluted 1:500, human anti-CREST (15-235, Antibodic sinc), 1:100, Rabbit
960 anti-CENP-E (C7488, Sigma Aldrich), diluted 1:100, Rabbit anti-Aurora B (ab239837,
961 Abcam), diluted 1:100, anti-Hec1 (ab3613, Abcam), diluted 1:100, anti-Spindly (A301-354A,
962 Biomolecules), diluted 1:100, anti-phospho-CENP-A (Ser7) (07-232, Sigma-Aldrich), diluted
963 1:500. After primary antibody, cells were washed in PBS and then incubated in 500 µL of
964 secondary antibody solution for 45 min at room temperature. The following secondary
965 antibodies were used: donkey anti-mouse IgG Alexa Fluor 594, diluted 1:250 (ab150112,
966 Abcam, Cambridge, UK), donkey anti-rabbit IgG Alexa Fluor 647 (ab150075, Abcam) and
967 donkey anti-rat IgG Alexa Fluor 647 (ab150155, Abcam), Goat anti-human IgG 594 (ab96909,
968 Abcam), all diluted 1:500. Finally, cells were washed with 1 mL of PBS, 3 times for 10 min.
969 This fixation was used for imaging HeLa PRC1-GFP cell line for siRNA silencing control,
970 kinetochore and PRC1 visualization in vertical rosettes and for PRC1 visualization in different
971 treatments (CENP-E overexpression, Aurora B relocalization) in untransfected HeLa cells.
972 To visualize alpha-tubulin in STED resolution in HeLa PRC1-GFP cell line, ice-cold
973 methanol protocol was avoided because it destroyed the unstable fraction of microtubules.
974 Cells were washed with cell extraction buffer (CEB) and fixed by a microtubule-preserving
975 mixture of 3.2% paraformaldehyde (PFA) and 0.25% glutaraldehyde (GA) in microtubule-

976 stabilizing PEM buffer (0.1 M PIPES, 0.001 M MgCl2 x 6 H2O, 0.001 M EDTA, 0.5 % Triton-
977 X-100) for 10 min at room temperature (Heuser and Kirschner, 1980). After fixation with PFA
978 and GA, for quenching, cells were incubated in 1 mL of freshly prepared 0.1% borohydride in
979 PBS for 7 min and after that in 1 mL of 100 mM NH_4Cl and 100 mM glycine in PBS for 10
980 min at room temperature. To block unspecific binding of antibodies, cells were incubated in
981 500 µL blocking/permeabilization buffer (1% normal goat serum and 0.5% Triton-X-100 in
982 water) for 2 hours at room temperature. Cells were then incubated in 500 µL of primary
983 antibody solution overnight at 4°C. After the incubation with a primary antibody, cells were
984 washed 3 times for 10 minutes with 1 ml of PBS and then incubated with 500 µl of secondary
985 antibody for 2 hours at room temperature. This protocol was used in all experiments where
986 tubulin is visualized in STED mode. In all fixations, DAPI (1 µg/mL) was used for
987 chromosome visualization.
988
989 **Imaging**
990 *STED microscope system (Abberior Instruments)*. STED microscopy was performed using the
991 Expert Line easy3D STED microscope system (Abberior Instruments) with a 60x/1.2
992 UPLSAPO 60XW water objective (Olympus), avalanche photodiode (APD) detector, and
993 Imspector software to acquire spindle cross-sections in horizontally and vertically oriented
994 spindles in different stages of mitosis of HeLa cells expressing PRC1-GFP, immunostained for
995 tubulin, with DNA stained by DAPI. STED images of tubulin were acquired in a single plane
996 in the Alexa 594 channel with the excitation and depletion laser power at 35%, and pixel size
997 set 20 nm. PRC1 and DNA were imaged in the same spindles in the confocal mode. Confocal
998 mode was also used to image fixed prometaphase rosettes and metaphase spindles in
999 untransfected and PRC1-GFP HeLa cells using eGFP and DAPI excitation lasers to visualize
1000 GFP and DAPI, respectively, or Alexa 488, 594, 647 excitation lasers depending on the
1001 secondary antibody. The laser power was 10%, except for Alexa 647 where it was 5%. Pixel
1002 size was 50 nm for prometaphase spindles and for imaging bridging fibers in metaphase, and
1003 100 nm for metaphase spindles. Z-stacks of 41 focal planes, except in experiments on lagging
1004 kinetochores where the number of planes was 20, were acquired with 0.5 µm spacing to cover
1005 the whole spindle. For live cell imaging of vertical metaphase spindles in HeLa PRC1-GFP
1006 cell line, the middle plane was recognized as the plane in which the bundles appear as clear
1007 dots of PRC1-GFP and the spindle cross-section is filled with chromosomes. Four planes close
1008 to the spindle midplane were acquired, separated by 0.5 µm. Pixel size was 50 nm. Laser power
1009 for eGFP excitation laser was 15%, and for SiR-DNA was 5%. Live cell imaging of horizontal

1010 metaphase spindles was performed in HeLa PRC1-GFP cell line with Z-stacks of 41 planes
1011 using eGFP excitation light at 10% laser power and 5% laser power for SiR-DNA channel.
1012 Pixel size was 100 nm. The bundling assay was applied for imaging of tubulin with SiR-tubulin
1013 dye in HeLa PRC1-GFP cell line. Time-lapse images of the spindle midplane were acquired
1014 using only SiR excitation laser with 8% power. Time between repetitions was 1 minute and
1015 pixel size was 100 nm.

1016 *Dragonfly spinning disk confocal microscope system (Andor Technology).* To image
1017 the formation of PRC1-labeled bundles in HeLa cells expressing PRC1-GFP (bundling assay),
1018 confocal live-cell imaging was performed on a Dragonfly spinning disk microscope (Andor
1019 Technology, Belfast) using 63x/1.47 HC PL APO glycerol objective (Leica, Belfast) and Zyla
1020 4.2P scientific complementary metal oxide semiconductor (sCMOS) camera (Andor
1021 Technology). Images were acquired using Fusion software. During imaging, cells were
1022 maintained at 37ºC and 5% CO_2 within a heating chamber (Okolab, Pozzuoli, NA, Italy). Only
1023 cells with vertically oriented spindles were imaged as follows: first a 41 plane Z-stack was
1024 acquired to cover the whole spindle using both 478 nm and 640 nm excitation light at a 10%
1025 and 5% laser power, respectively. Then a time-series of images was required using only 478
1026 nm excitation light. Every repetition recorded 9 middle frames of the vertical spindle, forming
1027 a stack of 9 slices separated 0.5 µm. Time between repetitions was 5.4 seconds. After the time-
1028 series, the second Z-stack was acquired, again using both excitation lasers. Total time-lapse
1029 movie was 9 minutes long. The same protocol was used for experiments with untreated cells,
1030 Haus6-depleted cells, and cells treated with Barasertib, GSK-923295, and nocodazole. For
1031 Ndc80, Haus6, and Spindly silencing control, a 41 plane Z-stack was acquired to cover the
1032 whole spindle using 478 nm, 620 nm and 408 nm excitation light at a 10% for first two and 5%
1033 laser power for DAPI channel. For all images pixel size was 100 nm.

1034 *Opterra confocal microscope system (Bruker).* For counting the number of bundles and
1035 for bundle trajectories, HeLa cells expressing PRC1-GFP and hTERT-RPE1 cells expressing
1036 CENP-A-GFP and Centrin1-GFP were imaged using Bruker Opterra Multipoint Scanning
1037 Confocal Microscope (Bruker Nano Surfaces, Middleton, WI, USA). The system was mounted
1038 on a Nikon Ti-E inverted microscope equipped with a Nikon CFI Plan Apo VC 100x/1.4
1039 numerical aperture oil objective (Nikon, Tokyo, Japan). The system was controlled with the
1040 Prairie View Imaging Software (Bruker). During imaging, cells were maintained at 37°C in
1041 Okolab Cage Incubator (Okolab, Pozzuoli, NA, Italy). For optimal resolution and signal-to-
1042 noise ratio, 22 nm slit was used. For excitation of GFP, 488 nm diode laser line was used. The
1043 excitation light was separated from the emitted fluorescence by using Opterra Dichroic and

1044 Barrier Filter Set 405/488/561/640. Images were captured with an Evolve 512 Delta Electron
1045 Multiplying Charge Coupled Device (EMCCD) Camera (Photometrics, Tucson, AZ, USA)
1046 using 150-200 ms exposure times. For counting the number of bundles, Z-stacks of 41 focal
1047 planes were acquired with 0.5 µm spacing to cover the whole spindle. Horizontally oriented
1048 prometaphase spindles of HeLa PRC1-GFP cells with added SiR-DNA dye and hTERT-RPE1
1049 cells expressing CENP-A-GFP and Centrin1-GFP with added SiR-tubulin dye were filmed
1050 every 10 and 5 minutes, respectively. Prometaphase cells were recognized by non-congressed
1051 chromosomes and relatively small spindle size. To image the dynamics of PRC1-labeled
1052 bundles in HeLa cells expressing PRC1-GFP, confocal live-cell imaging was performed. Only
1053 cells with vertically oriented spindles were imaged as follows: first a 41 plane Z-stack was
1054 acquired to cover the whole spindle using both 488 nm and 640 nm excitation light. Then a
1055 time-series of images was required using only 488 nm excitation light. Every repetition
1056 recorded 9 middle frames of the vertically oriented spindle, forming a stack of 9 slices separated
1057 0.5 µm. Time between repetitions was 2.7 seconds. After the time-series, a second Z-stack was
1058 acquired, again using both excitation lasers. Total time lapse movie was 4.5 minutes long. Laser
1059 powers were 10% and 5% for 488 nm and 640 nm excitation light, respectively.
1060
1061 **Image processing and data analysis**
1062 All images were analyzed in Fiji/ImageJ (National Institutes of Health, Bethesda, MD, USA).
1063 Raw images were used for quantification. Contrast was adjusted for clarity of presentation in
1064 the figures. MatLab (MathWorks, Natick, MA, USA) was used to create the plots, Rstudio (R
1065 Foundation for Statistical Computing, Vienna, Austria) to transform the horizontally oriented
1066 spindles into an end-on view. Figures were assembled in Adobe Illustrator CS5 (Adobe
1067 Systems, Mountain View, CA, USA).
1068 *Bundling assay.* For analysis of bundle formation, Squash plugin in Fiji was used in the
1069 PRC1-GFP channel of the middle plane of the spindle. Segmentation was performed using
1070 Squash [95]. In the main graphical user interface Squash window, we set the parameter for
1071 background subtraction option, entering the window edge lengths in units of 14 pixels. Object
1072 detection was performed over the entire image. The higher value of the regularization
1073 parameter of 0.1 was used to avoid the segmenting noise-induced small intensity peaks.
1074 Intensity values were normalized between 0 for the smallest value occurring in the image, and
1075 1 for the largest value. The sub-pixel segmentation was selected. The resolution of the
1076 segmentation was increased by an oversampling factor of 8 for 2D images. Local intensity
1077 estimation parameter was set to automatic. The Poisson model, recommended for confocal

1078 microscopes, was chosen. The following visualization options were selected: object intensities,
1079 number of objects and the mean object size in terms of area. Validation was performed by
1080 manually measuring object segmentation in the middle plane of a representative spindle.

1081 *Number of bundles.* To count the bundles, horizontally oriented spindles were
1082 transformed into vertical (end-on) orientation using the code written in R programming
1083 language in R Studio (R Core Team., 2016). Before the transformation, the Z-stack of the
1084 spindle in a single channel was rotated in Fiji so that the spindle major axis was approximately
1085 parallel to the x-axis. The aberrations caused by refractive index mismatch between immersion
1086 oil and aqueous sample were taken into account in the program by multiplying Z-step size by
1087 a correction factor of 0.81 to obtain the correct Z-distance. This factor corresponds to the ratio
1088 of the cell diameter in y and z direction, assuming that a mitotic cell is spherical. Bundles were
1089 counted on the sum intensity images of 5 central planes of the transformed spindle. The number
1090 of bundles was determined by counting the bright spots using Multi point tool in ImageJ.

1091 *Protein silencing*. Analysis of the immunofluorescence signal was performed on the
1092 sum of all 41 planes. The territory of the spindle was encircled with a segmented line in Fiji
1093 and sum intensity was measured.

1094 *PRC1 intensity of early formed bundles in the prometaphase rosette.* To measure the
1095 bundle intensity in vertically oriented early prometaphase rosette, bundles were encircled in
1096 Fiji and sum intensity was measured in only one plane of the cross section where the bundle
1097 was of highest intensity. Bundles with bound kinetochores were measured in the plane where
1098 the kinetochore was visible close to the bundle. The brightest bundles (usually two) that
1099 connect the spindle poles in a straight line were not measured because they are formed before
1100 nuclear envelope breakdown. Thus, only bundles in the prometaphase network were measured.

1101 *PRC1 intensity of bundles in metaphase.* To measure the bundle intensity in vertically
1102 oriented metaphase spindles, each bundle was encircled in Fiji with a fixed-size circle (p=0.61
1103 μm^2) and mean intensity was measured in only one plane of the cross-section where DNA
1104 covered the whole cross-section. To calculate the PRC1 intensity of the bundle, mean intensity
1105 of PRC1 in the cytoplasm was subtracted from bundle PRC1 intensity. Furthermore, to correct
1106 for the differences in PRC1 expression in different cells, the PRC1 bundle intensity was divided
1107 by the mean intensity of PRC1 in the cytoplasm to get the normalized PRC1 intensity.

1108 *PRC1 intensity of the network in early prometaphase.* To measure the network intensity
1109 in vertically oriented prometaphase spindles, the region excluding the brightest bundles (the
1110 ones formed before nuclear envelope breakdown) was encircled in Fiji and mean intensity was
1111 measured in only one plane. As for the PRC1 intensity of bundles, the mean intensity of PRC1

1112 in the cytoplasm was subtracted from the network PRC1 intensity, and the result was divided
1113 by the mean intensity of PRC1 in the cytoplasm to get the normalized PRC1 intensity.
1114 *Tubulin intensity of bridging fibers in metaphase.* Intensity of bridging fibers was
1115 measured on metaphase spindles. A line was drawn along the bridging fiber using Line tool in
1116 Fiji, only the region beneath the kinetochore pair was measured. Intensity of tubulin was
1117 measured at the midpoint of the line intensity plot. Furthermore, to correct for the differences
1118 in tubulin signal in different cells, tubulin bundle intensity was divided by the mean intensity
1119 of tubulin in the cytoplasm to get the normalized tubulin intensity.
1120 *PRC1 line intensity in metaphase.* In HeLa PRC1-GFP cell line, a line was drawn from
1121 pole to pole in a metaphase spindle, which was recognized by fully aligned chromosomes in
1122 control cells. In treatments that cause impaired chromosome congression, spindles with most
1123 chromosomes aligned were chosen. Line intensity plot was made by subtracting the
1124 cytoplasmatic PRC1 signal and dividing by it, providing the normalized PRC1 intensity.
1125 *Aurora B-PRC1 correlation.* Individual PRC1-labeled bridging fibers were encircled
1126 with a circle that goes from the top edge of the bundle to the bottom edge, and the sum intensity
1127 was measured. The same-size circle was used to measure the sum intensity of the Aurora B
1128 signal on the associated centromere. Normalized intensity of PRC1 and Aurora B was obtained
1129 by subtracting the cytoplasmatic mean intensity of the respective protein and dividing by it.
1130 *Phosphorylation of outer kinetochore.* Sum intensity of CREST and CENP-A signal
1131 was measured in prometaphase cells. The spindle was boxed in a fixed square that was same
1132 for all cells. The intensity ratio was expressed by dividing the CENP-A-Ser7P sum intensity
1133 by the CREST sum intensity.
1134 *Spindle parameters.* Spindle width and length were measured on horizontally oriented
1135 metaphase spindles using Line tool in Fiji.
1136 *Manual bundle tracking.* The 2D trajectories of the bundles and their coordinates were
1137 tracked using Manual tracking tool to obtain bundle trajectories. The movement of all bundles
1138 was represented with respect to the brightest bundle(s) that appear before nuclear envelope
1139 breakdown and do not have chromosomes attached in early prometaphase, using Manual drift
1140 correction plugin in Fiji.
1141 *DNA occupancy in the metaphase.* Sum intensity of SiR-DNA signal from 41 planes
1142 was used for measurement of DNA occupancy in the equatorial region of the spindle.
1143 Proportion of DNA at the metaphase plate over time was measured as mean intensity of the
1144 DNA within the line covering the equatorial region divided by the intensity of all DNA in the
1145 cell. The line covering the equatorial region was defined in metaphase so that its width was

1146 equal to the width of the metaphase plate and length equal to spindle width. The same line was
1147 used for all time frames.
1148 *Lagging kinetochores* were identified by the CREST signal together with the DNA
1149 signal in the central part of the spindle in anaphase, between the two segregated groups of
1150 kinetochores/chromosomes.
1151 *Statistical analysis and figure preparation.* Graphs were generated in Matlab
1152 (MathWorks, Natick, MA, USA). Fiji was used to scale images and adjust brightness and
1153 contrast. Figures were assembled in Illustrator (Adobe Systems, Mountain View, CA, USA).
1154 Data are given as mean ± s.e.m., unless otherwise stated. Means of two groups were compared
1155 by Student's t-test (two-tailed and two-sample unequal-variance), and means of more than two
1156 groups by one-way ANOVA test and Tukey's HSD post hoc test, $p < 0.05$ was considered
1157 statistically significant. The numbers of microtubule bundles, cells, and independent
1158 experiments are given in the figure panels.
1159

Theoretical model

To describe the dynamical transition from array like distribution of microtubules to well organized multiple bundles during prometaphase, we consider both equilibrium and non equilibrium processes involving microtubules, crosslinking proteins, chromosomes, and kinetochores. The model we construct is placed in an one dimensional geometry with spatial coordinate x, taken from the part of the circumference of the disc that is obtained by taking a vertical cross section at the mid plane of a prometaphase spindle as shown in Fig 5A. Microtubules and crosslinkers are described as point like objects with densities $\tilde{\rho}$ and $\tilde{\psi}$, respectively. For simplicity, we assume that crosslinker have a uniform density.

In our model, we include interactions between microtubules, crosslinkers and kinetochores. We describe these interactions by constructing a Landau–Ginzburg free energy:

$$F[\tilde{\rho}] = \int d\tilde{x}\Big\{\frac{\tilde{w}}{4}\tilde{\rho}^4 + \frac{\tilde{\kappa}}{2}\Big(\frac{\partial\tilde{\rho}}{\partial\tilde{x}}\Big)^2 - \tilde{\zeta}\tilde{\rho}\tilde{\psi}\tilde{\rho} - \tilde{\alpha}\tilde{\rho}^2\delta(\tilde{x} \pm (2n+1)\tilde{d})\Big\}. \tag{1}$$

In the first term we describe local microtubule repulsion as nonlinear interaction with strength $\tilde{w}$. The second term captures a non-local repulsion of strength $\tilde{\kappa}$, which is coming from interaction between chromosomes and microtubules. The third term describes an attractive interaction between two microtubules mediated by crosslinkers and with coupling constant $\tilde{\zeta}$. The last term represents attraction between kinetorchores and microtubules of strength $\tilde{\alpha}$. This local attraction is described by Dirac delta function. In our system, kinetochores are placed in regular intervals of given integer index n, forming lattice-like structure with spacing $2\tilde{d}$.

Time evolution of microtubule density can be obtained by writing a conserved dynamics of $\tilde{\rho}$ by minimizing $F[\tilde{\rho}]$ and incorporating non equilibrium process of appearance and disappearance of microtubules in our region of interest. Rapid polymerization and depolymerization of microtubule filaments causes the processes of creation and annihilation of those filaments in the mid plane of the vertically oriented spindle. We assume that microtubules are created with a constant rate ω_{on} and get disassembled with a rate ω_{off}. Finally, we calculate how microtubule density changes in time t as

$$\frac{\partial\tilde{\rho}}{\partial t} = \tilde{w}\tilde{M}_\rho\frac{\partial^2\tilde{\rho}^3}{\partial\tilde{x}^2} - \tilde{\kappa}\tilde{M}_\rho\frac{\partial^4\tilde{\rho}}{\partial\tilde{x}^4} - 2\tilde{\zeta}\tilde{M}_\rho\tilde{\psi}\tilde{M}_\rho\frac{\partial^2\tilde{\rho}}{\partial\tilde{x}^2} - 2\tilde{\alpha}\tilde{M}_\rho\frac{\partial^2}{\partial\tilde{x}^2}\{\tilde{\rho}\delta(\tilde{x} \pm (2n+1)\tilde{d})\} + \omega_{on}\tilde{\rho}_b - \omega_{off}\tilde{\rho}$$

Here, $\tilde{\rho}_b$ denotes microtubule nucleation density in the cytoplasm and $\tilde{M}_\rho$ is microtubule mobility. Now, we proceed to make this time evolution equation dimensionless by using a length scale $x = \tilde{x}(\tilde{w})^{-\frac{1}{3}}$ and a time scale $\tau = t\omega_{off}$ and obtain,

$$\frac{\partial\rho}{\partial\tau} = M_\rho\frac{\partial^2\rho^3}{\partial x^2} - \kappa M_\rho\frac{\partial^4\rho}{\partial x^4} - 2\zeta M_\rho\psi\frac{\partial^2\rho}{\partial x^2} - 2\bar{\alpha}M_\rho\frac{\partial^2}{\partial x^2}\{\rho\delta(x \pm (2n+1)d)\} + \omega\rho_b - \rho, \tag{2}$$

where $\rho = \tilde{\rho}\tilde{w}^{\frac{1}{3}}$, $\psi = \tilde{\psi}\tilde{w}^{\frac{1}{3}}$, $\zeta = \tilde{\zeta}\tilde{w}^{-\frac{2}{3}}$, $\kappa = \tilde{\kappa}\tilde{w}^{-1}$, $\bar{\alpha} = \tilde{\alpha}\tilde{w}^{-1}$, $d = \tilde{d}\tilde{w}^{-\frac{1}{3}}$, $\rho_b = \tilde{\rho}_b\tilde{w}^{\frac{1}{3}}$, $M_\rho = \tilde{M}_\rho\omega_{off}^{-1}$ and $\omega = \frac{\omega_{on}}{\omega_{off}}$.

A. Boundary conditions and steady state density profiles

To study the kinetochore driven bundling of microtubules in the linear regime, we construct linearized steady state equation with steady state microtubule density ρ_f from Eq.(2) by setting $\rho = \rho_s + \rho_f$, where $\rho_s = \frac{\omega_{on}}{\omega_{off}}\rho_b$. The steady state equation with delta-function at $\pm d$ reads as

$$M_\rho\Big[(3\rho_s^2 - 2\zeta\psi)\frac{\partial^2\rho_f}{\partial x^2} - \kappa\frac{\partial^4\rho_f}{\partial x^4}\Big] - \rho_f - 2\bar{\alpha}M_\rho\frac{\partial^2}{\partial x^2}\{(\rho_s + \rho_f)\delta(x \pm d)\} = 0 \tag{3}$$

The last term in Eq.(3) is vanishing at all positions except at $\pm d$. Thus, we first solve Eq.(3) between boundary points by searching for solutions in the form $\rho_f(x) = \sum_{j=1}^{4} C_j e^{-im_j x}$ and obtain

$$m^4 + \eta_1 m^2 + \eta_2 = 0, \tag{4}$$

where, $\eta_1 = \frac{3\rho_s^2 - 2\zeta\psi}{2\kappa}$ and $\eta_2 = \frac{1}{\kappa M_\rho}$. Symmetry of Eq.(4) ensures the four solution $m_{1,2,3,4}$ can be written as $m_3 = -m_1$ and $m_4 = -m_2$ and consequently we obtain the density profile in steady state as

$$\rho_f(x) = C_1 e^{-im_1 x} + C_2 e^{-im_2 x} + C_3 e^{im_1 x} + C_4 e^{im_2 x}, \tag{5}$$

$C_{1,..,4}$ being constants of integration. The structure of the system with two attractive δ functions at $\pm d$ ensures the existence of mirror symmetry $\rho_f(-x) = \rho_f(x)$ and Eq.(5) reduces to,

$$\rho_f(x) = C_1(e^{im_1 x} + e^{-im_1 x}) + C_2(e^{im_2 x} + e^{-im_2 x}) \tag{6}$$

Performing repeated integration of Eq.(3) and finally in the $\lim_{\epsilon \to 0}$, $\int_{d-\epsilon}^{d+\epsilon}$ around the δ function yields,

$$\kappa[\rho_f'(-d) - \rho_f'(d)] + 2\bar{\alpha}\rho_s + 2\bar{\alpha}\rho_f(d) = 0 \tag{7}$$

Here, we have used the translational invarience of the density $\rho(x + 2d) = \rho(x)$. Eq.(7) implies a discontinuous change in the first derivative of ρ_f at $\pm d$. Similarly, between two boundaries, where the attractive interaction due to kinetochore is absent one obtains by integrating Eq.(3)

$$\left[\frac{\partial^3 \rho_f}{\partial x^3}\right]_{-d}^{d} - \eta_1 \left[\frac{\partial \rho_f}{\partial x}\right]_{-d}^{d} + \eta_2 \int_{-d}^{d} \rho_f(x)\, dx = 0 \tag{8}$$

Eq.(6), Eq.(7), and Eq.(8) altogether give us the full density profiles depending on the nature of the roots m_1 and m_2.

When m_1 and m_2 are purely imaginary, we have

$$\begin{aligned} \rho_f(x) &= 2C_1 cosh(m_1 x) + 2C_2 cosh(m_2 x), \\ C_1 &= \frac{\rho_s}{2[\frac{\kappa}{\bar{\alpha}} m_1 sinh(m_1 d) - cosh(m_1 d)] - 2\frac{P_1}{Q_1}[\frac{\kappa}{\bar{\alpha}} m_2 sinh(m_2 d) - cosh(m_2 d)]}, \\ C_2 &= -\frac{\rho_s}{2\frac{Q_1}{P_1}[\frac{\kappa}{\bar{\alpha}} m_1 sinh(m_1 d) - cosh(m_1 d)] - 2[\frac{\kappa}{\bar{\alpha}} m_2 sinh(m_2 d) - cosh(m_2 d)]} \end{aligned} \tag{9}$$

with $P_1 = sinh(m_1 d)\{m_1^3 - m_1\eta_1 + \frac{\eta_2}{m_1}\}$ and $Q_1 = sinh(m_2 d)\{m_2^3 - m_2\eta_1 + \frac{\eta_2}{m_2}\}$.

As m_1 and m_2 become a pair of complex conjugate roots written as $m_1 = a + ib$ and $m_2 = a - ib$, we obtain a density profile given by

$$\begin{aligned} \rho_f(x) &= 4C cosh(bx) cos(ax) + 4\bar{C} sinh(bx) sin(ax), \\ C &= \frac{\rho_s}{4\frac{P_2}{Q_2}[\beta_2 - \frac{\kappa}{\bar{\alpha}}(b\alpha_1 + a\beta_1)] - 4[\alpha_2 + \frac{\kappa}{\bar{\alpha}}(a\alpha_1 - b\beta_1)]}, \\ \bar{C} &= -\frac{\rho_s}{4[\beta_2 - \frac{\kappa}{\bar{\alpha}}(b\alpha_1 + a\beta_1)] - 4\frac{Q_2}{P_2}[\alpha_2 + \frac{\kappa}{\bar{\alpha}}(a\alpha_1 - b\beta_1)]} \end{aligned} \tag{10}$$

where $C = C_1 + C_2$, $\bar{C} = C_1 - C_2$, $\alpha_1 = cosh(bd)sin(ad)$, $\beta_1 = sinh(bd)cos(ad)$, $\alpha_2 = cosh(bd)cos(ad)$, $\beta_2 = sinh(bd)sin(ad)$, $P_2 = \alpha_1\{a(a^2 - -3b^2)\} + \beta_1\{b(b^2 - 3a^2)\} + \eta_1(a\alpha_1 - b\beta_1) + \frac{\eta_2}{a^2+b^2}(a\alpha_1 + b\beta_1)$, and $Q_2 = \alpha_1\{b(b^2 - 3a^2)\} - \beta_1\{a(a^2 - -3b^2)\} - \eta_1(b\alpha_1 + a\beta_1) + \frac{\eta_2}{a^2+b^2}(b\alpha_1 - a\beta_1)$.

For real m_1 and m_2 we have,

$$\begin{aligned}
\rho_f(x) &= 2C_1 cos(m_1 x) + 2C_2 cos(m_2 x), \\
C_1 &= \frac{\rho_s}{2[\frac{\kappa}{\bar{\alpha}} m_1 sin(m_1 d) + cosh(m_1 d)] - 2\frac{P_3}{Q_3}[\frac{\kappa}{\bar{\alpha}} m_2 sin(m_2 d) + cos(m_2 d)]}, \\
C_2 &= -\frac{\rho_s}{2\frac{Q_3}{P_3}[\frac{\kappa}{\bar{\alpha}} m_1 sin(m_1 d) + cos(m_1 d)] - 2[\frac{\kappa}{\bar{\alpha}} m_2 sin(m_2 d) + cos(m_2 d)]}
\end{aligned} \tag{11}$$

with $P_3 = sin(m_1 d)\{m_1^3 + m_1\eta_1 + \frac{\eta_2}{m_1}\}$ and $Q_3 = sin(m_2 d)\{m_2^3 + m_2\eta_1 + \frac{\eta_2}{m_2}\}$.

ACKNOWLEDGEMENTS

We thank Ina Poser, Tony Hyman, Alexey Khodjakov, Marin Barišić, Casper Hoogenraad, and Neda Slade for cells, plasmids, and chemicals, Ivana Šarić for the drawings, and all members of Tolić and Pavin groups for helpful discussions. This work was funded by the European Research Council (ERC Synergy Grant, GA Number 855158, granted to I.M.T. and N.P.), the Croatian Science Foundation (HRZZ, project PZS-2019-02-7653 granted to I.M.T.), and projects co-financed by the Croatian Government and European Union through the European Regional Development Fund — the Competitiveness and Cohesion Operational Programme: IPSted (Grant KK.01.1.1.04.0057) and QuantiXLie Center of Excellence (grant KK.01.1.1.01.0004).

AUTHOR CONTRIBUTIONS

J.M. performed and analyzed all experiments, except the experiments with lagging kinetochores and PRC1 and CENP-E overexpression, which were done by M.Ć. S.G. developed the theoretical model. I.M.T. and N.P. conceived the project and supervised the experimental and theoretical work, respectively. I.M.T., J.M., and N.P. wrote the paper with input from all authors.

COMPETING INTERESTS

The authors declare no competing interests.

1182 **SUPPLEMENTARY MATERIALS**

1183

Supplementary Figure 1

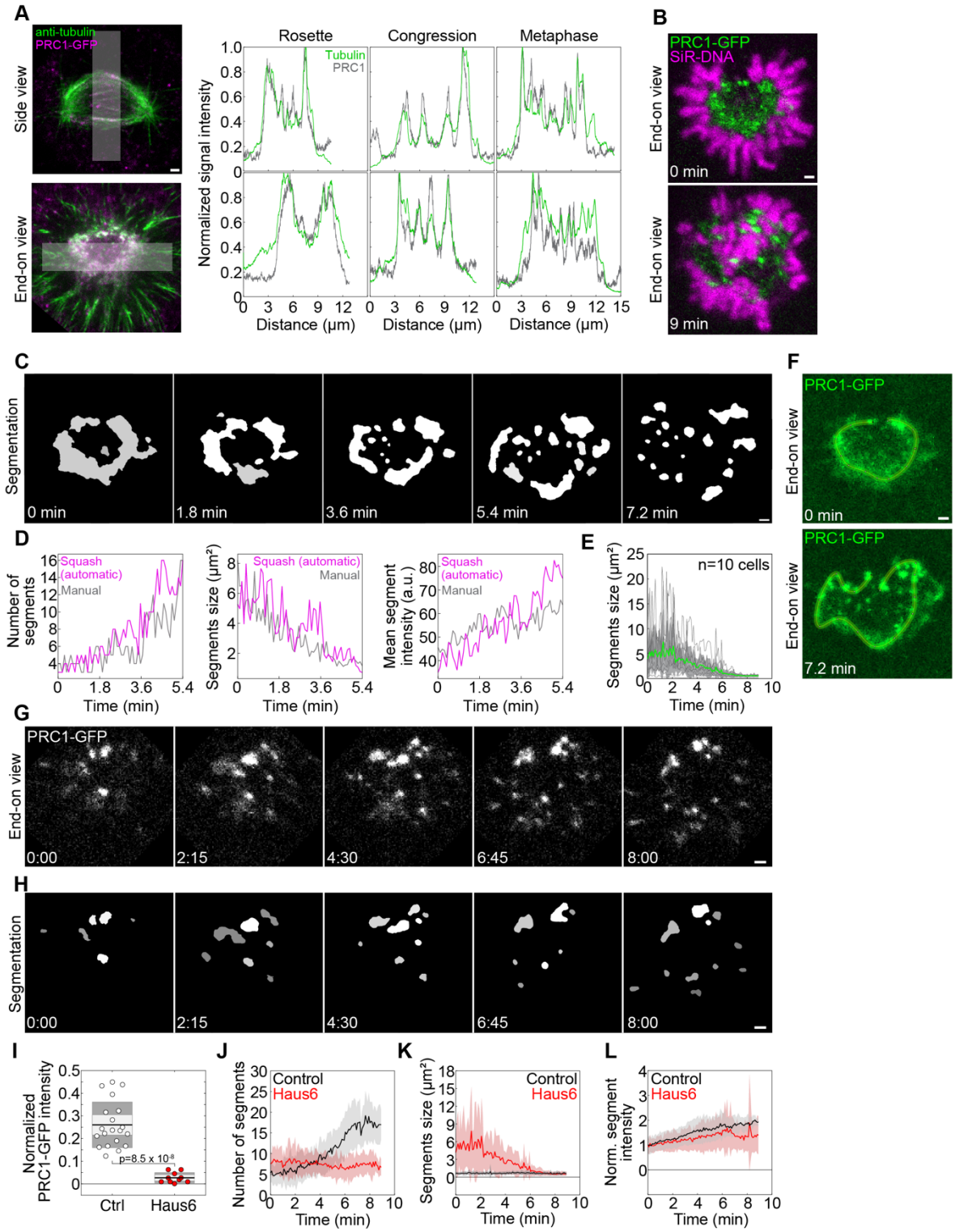

1184

1185 **Extended Data Fig. 1: Additional characterization of the network-to-bundles transition**
1186 **of PRC1-crosslinked microtubules.**
1187 **a**, STED images of tubulin (green) and confocal images of PRC1 (magenta) from Fig. 1a, with
1188 superimposed lines drawn in Fiji (left) used to measure line intensity profiles on horizontally
1189 oriented spindles (top), and vertically oriented spindles (bottom) in different phases as
1190 indicated (right). Both PRC1-GFP and anti-tubulin intensity profiles are shown. Intensity is
1191 normalized to the maximum value. Note the colocalization of the PRC1 and tubulin signal. **b**,
1192 Midplane of a vertically oriented spindle in a HeLa-Kyoto BAC cell stably expressing PRC1-
1193 GFP (green) with DNA labeled by SiR-DNA (magenta), before (top) and after (bottom)
1194 antiparallel bundle formation (9 minutes). **c**, Squash segmentation results for time-lapse images
1195 of the midplane of a vertically oriented prometaphase spindle in a HeLa-Kyoto BAC cell stably
1196 expressing PRC1-GFP corresponding to Fig. 1b. **d**, Validation of the squash segmentation
1197 method by manual measurements on a representative spindle. Graphs show the number of
1198 segments, their size and mean intensity (from left to right). **e**, Mean size of PRC1 segments in
1199 the midplane over time in HeLa-Kyoto BAC cells stably expressing PRC1-GFP, obtained using
1200 squash segmentation. Gray lines represent individual cells, green line the mean and gray areas
1201 the standard deviation (n=10 cells in 10 independent experiments). **f**, Lines drawn in Fiji along
1202 the periphery of the spindle midplane, where the PRC1 network is located in prometaphase,
1203 which were used to measure line intensity profiles in Fig. 1e,f. **g**, Time lapse images of the
1204 midplane (single plane) of a vertically oriented prometaphase spindle in a Haus6-depleted
1205 HeLa-Kyoto BAC cell stably expressing PRC1-GFP, starting with the prometaphase rosette.
1206 Time is shown in minutes:seconds. **h**, Squash segmentation results of the images shown in **g**.
1207 **i**, Mean intensity of PRC1-GFP in a region on the opposite side of the bundles that lack
1208 chromosomes in the early prometaphase network in control (n=20) and Haus6-depleted (n=10)
1209 HeLa cells expressing PRC1-GFP. PRC1-GFP intensity is normalized to the cytoplasmatic
1210 PRC1-GFP intensity. **j**, Number of PRC1 segments in the midplane over time in Haus6-
1211 depleted (red) and control (black, gray) HeLa-Kyoto BAC cells stably expressing PRC1-GFP
1212 (n=10 cells for control and 9 cells for Haus6 depletion), obtained using squash segmentation.
1213 Colored surfaces around the central lines (mean) represent standard deviation. **k**, Segment size
1214 and **l**, normalized segment intensity of PRC1-GFP segments from the same cells as in **j**. All
1215 scale bars, 1 µm.

Supplementary Figure 2

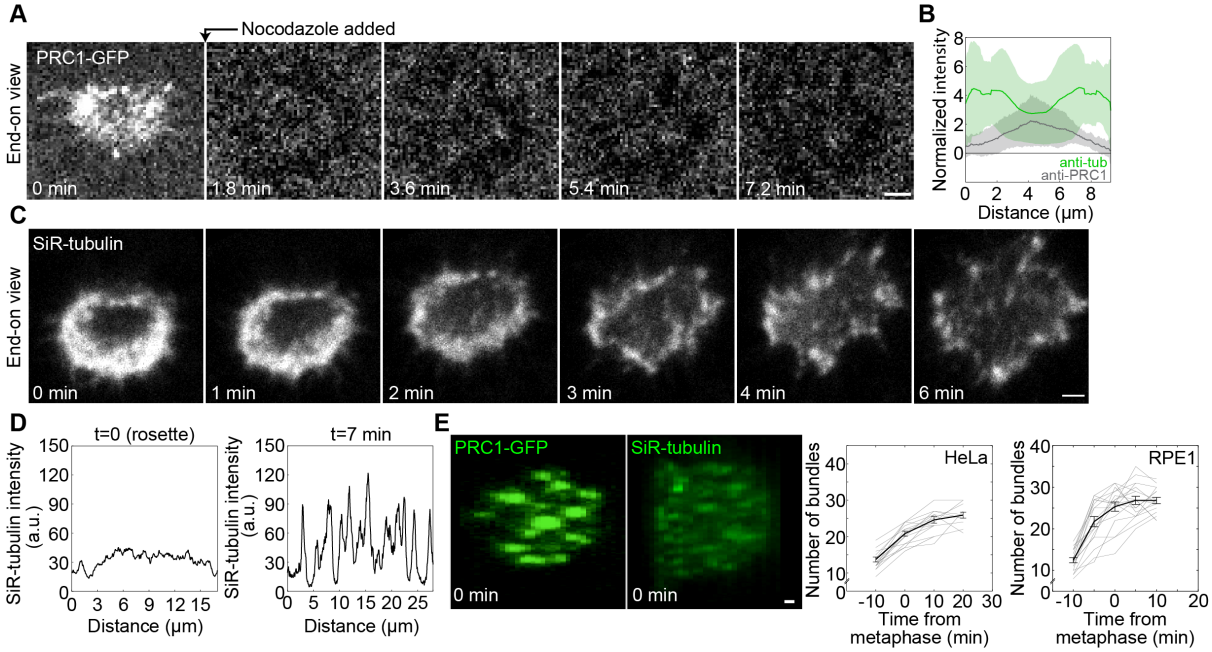

1216

1217

1218 **Extended Data Fig. 2: Additional characterization of PRC1 and tubulin during bundle**
1219 **formation.**

1220 **a**, Time lapse images of the midplane (single plane) of a vertically oriented prometaphase
1221 spindle in a HeLa-Kyoto BAC cell stably expressing PRC1-GFP, starting with the
1222 prometaphase rosette. Time when nocodazole was added is indicated. **b**, Intensity line plots of
1223 the anti-PRC1 (gray) and anti-tubulin (green) signal along the pole-to-pole axis in horizontally
1224 oriented early prometaphase spindles (rosette stage) of non-transfected immunostained HeLa
1225 cells, n=20 cells from 2 independent immunostainings. Intensity was normalized to the
1226 cytoplasmatic anti-PRC1 and anti-tubulin intensity, respectively. Note that the PRC1 intensity
1227 is highest in the middle of the spindle, whereas tubulin intensity is highest away from the
1228 middle, i.e., close to the poles. **c**, Time lapse images of the midplane (single plane) of a
1229 vertically oriented prometaphase spindle in a HeLa-Kyoto BAC cell stably expressing PRC1-
1230 GFP and stained with SiR-tubulin, starting with the prometaphase rosette. Only SiR-tubulin
1231 channel was imaged. **d**, SiR-tubulin intensity line plots along the periphery of the spindle
1232 midplane at t=0 and t=7 minutes from the cell shown in **c**. **e**, Reconstructed (rotated by 90
1233 degrees) images of the midplane of a horizontally oriented spindle in a HeLa-Kyoto BAC cell
1234 stably expressing PRC1-GFP (left image) and in an hTERT-RPE1 cell expressing CENP-A-
1235 GFP and centrin1-GFP labeled with SiR tubulin (right image). Graphs show the number of
1236 bundles over time for the HeLa cell line (left, n=12 cells) and the RPE1 cell line (right, n=16

1237 cells), corresponding to the images on the left. Time zero is the beginning of metaphase. All
1238 scale bars, 1 μm.

Supplementary Figure 3

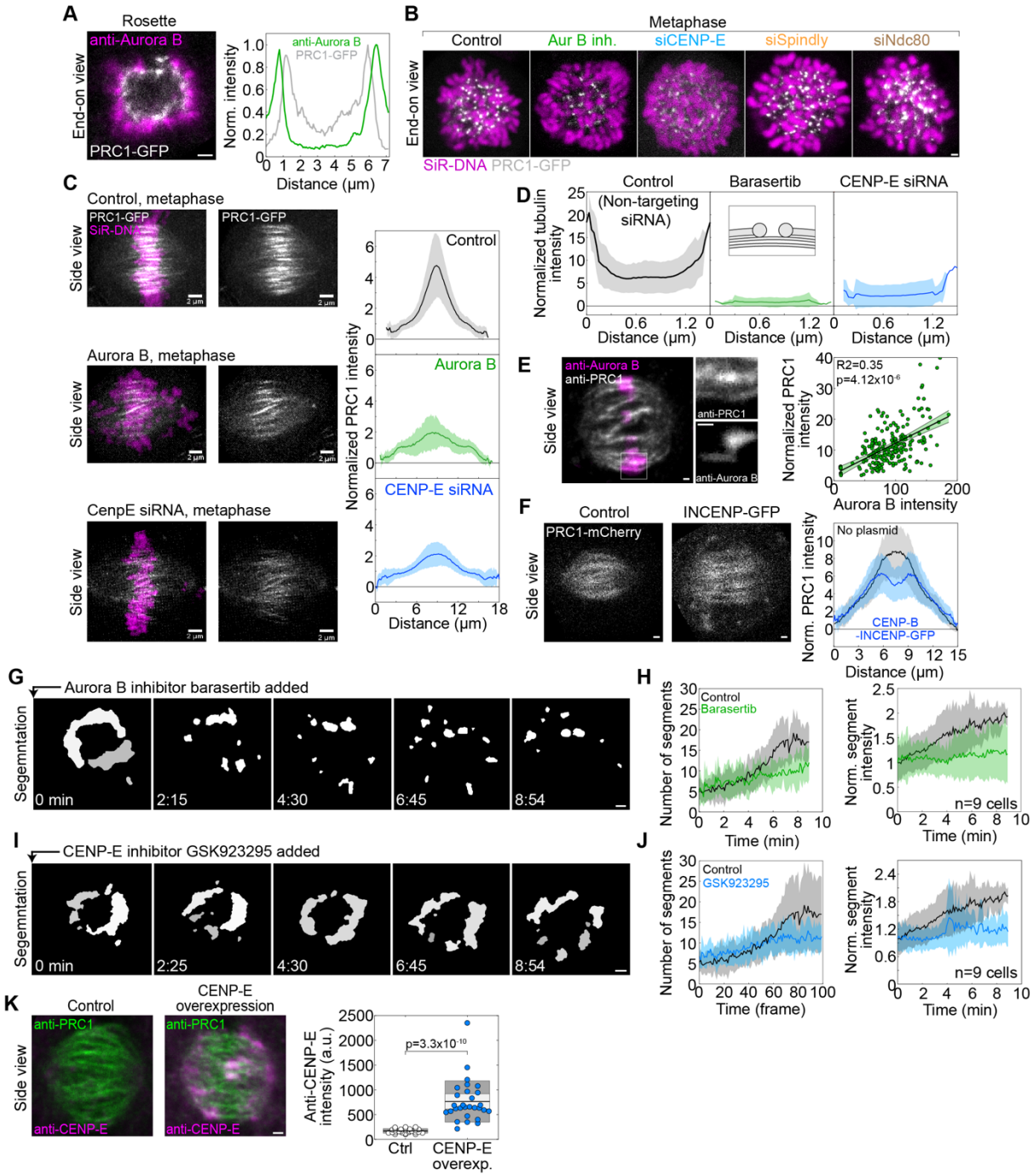

Extended Data Fig. 3: Additional characterization of the role of kinetochores in overlap bundle formation.

a, Left, image of a vertically oriented prometaphase rosette immunostained for Aurora B (magenta) in a HeLa-Kyoto BAC cell stably expressing PRC1-GFP (white). Right, intensity line plot of PRC1-GFP (grey) and anti-Aurora B (green) along a line drawn across the spindle cross-section, passing through the center. Line thickness was 1/3 of the spindle cross-section.

1247 Intensity is normalized to the maximum value for each channel. **b**, Images of vertically oriented
1248 metaphase spindles in a HeLa-Kyoto BAC cell line stably expressing PRC1-GFP (white) from
1249 Fig. 2e. Chromosomes are labeled with SiR-DNA (magenta) to show the metaphase plate. **c**,
1250 Live-cell images of horizontally oriented metaphase spindles in HeLa-Kyoto BAC cells stably
1251 expressing PRC1-GFP (white) and stained with SiR-DNA (magenta). Control (top), Aurora B
1252 inhibition (middle) and CENP-E depletion (bottom). Maximal projections of 41 planes are
1253 shown. The corresponding intensity line profiles of PRC1-GFP are shown to the right, mean
1254 (central line) and standard deviation (colored surface). The line profiles were measured along
1255 a line drawn from pole to pole. Line thickness was 1/3 of the spindle width. Intensity was
1256 normalized to the cytoplasmatic PRC1 intensity. Scale bars, 2 µm. Number of cells: 56 for
1257 control, 32 for Aurora B inhibition, 43 for CENP-E siRNA. All measurements are from 3
1258 independent experiments. **d**, Intensity line profiles corresponding to anti-tubulin signal in the
1259 bridging fiber from Fig. 2f,g and Fig. 3b,c; mean (central line) and standard deviation (colored
1260 surface); n=22 bundles from 14 cells for control, 11 bundles from 9 cells for Aurora B
1261 inhibition, and n=10 bundles from 7 cells for CENP-E siRNA, from 3 independent
1262 immunostainings. Intensity was normalized to the cytoplasmatic anti-tubulin intensity. **e**,
1263 Image of a spindle immunostained for Aurora B (magenta) and PRC1 (white) in an
1264 untransfected HeLa cell in metaphase. Sum of 5 planes is shown. Enlargements of anti-PRC1
1265 and anti-Aurora B (both in white) within the square marked on the main image are shown to
1266 the right. Graph shows correlation between anti-PRC1 and anti-Aurora B signal on the
1267 corresponding centromere, n=404 PRC1-Aurora B pairs from 26 cells. Intensity was
1268 normalized to the cytoplasmatic anti-PRC1 and anti-Aurora B intensity, respectively. **f**, Live
1269 cell images of metaphase spindles in HeLa cells transfected with PRC1-mCherry (white) in a
1270 control cell (left image) and a cell transfected with CENP-B-INCENP-GFP construct (right
1271 image). Maximal projections of 41 planes are shown. Graph shows intensity line plots of
1272 PRC1-mCherry along the spindle main axis, mean (central line) and standard deviation
1273 (colored surfaces), n=29 cells for control and n=28 for CENP-B-INCENP-GFP, 3 independent
1274 experiments per condition. Intensity was normalized to the cytoplasmatic PRC1 intensity. **g**,
1275 Squash segmentation results for time-lapse images of the midplane of a Barasertib-treated
1276 vertically oriented prometaphase spindle in a HeLa-Kyoto BAC cell stably expressing PRC1-
1277 GFP, corresponding to Fig. 2j. **h**, Number of PRC1 segments (left) and normalized mean
1278 intensity of PRC1 segments (normalized to the intensity at t=0, right) over time from squash
1279 segmentation in control and Barasertib-treated (i.e., Aurora B-inhibited) cells, as indicated.
1280 Colored surfaces around the central lines (mean) represent standard deviation, n=9 cells from

1281 9 independent experiments. **i**, Squash segmentation results and **j**, the related quantification for
1282 cells treated with the CENP-E inhibitor GSK923295, corresponding to Fig. 3f. Legend as in **g**
1283 and **h**, respectively, n=9 cells from 9 independent experiments. **k**, Images of horizontally
1284 oriented spindles in metaphase, immunostained for PRC1 (green) and CENP-E (magenta), in
1285 a control HeLa cell (left image) and after CENP-E overexpression (right image). Graph shows
1286 total CENP-E intensity on the spindle in control cells and after CENP-E overexpression, n=29
1287 cells in each condition from 3 independent experiments. The black line shows the mean; the
1288 light and dark grey areas mark 95% confidence interval on the mean and standard deviation,
1289 respectively. Note that the overexpression level is roughly 5-fold. In all controls for siRNA
1290 experiments the cells were transfected with nontargeting siRNA. All scale bars except in **c**, 1
1291 μm.

Supplementary Figure 4

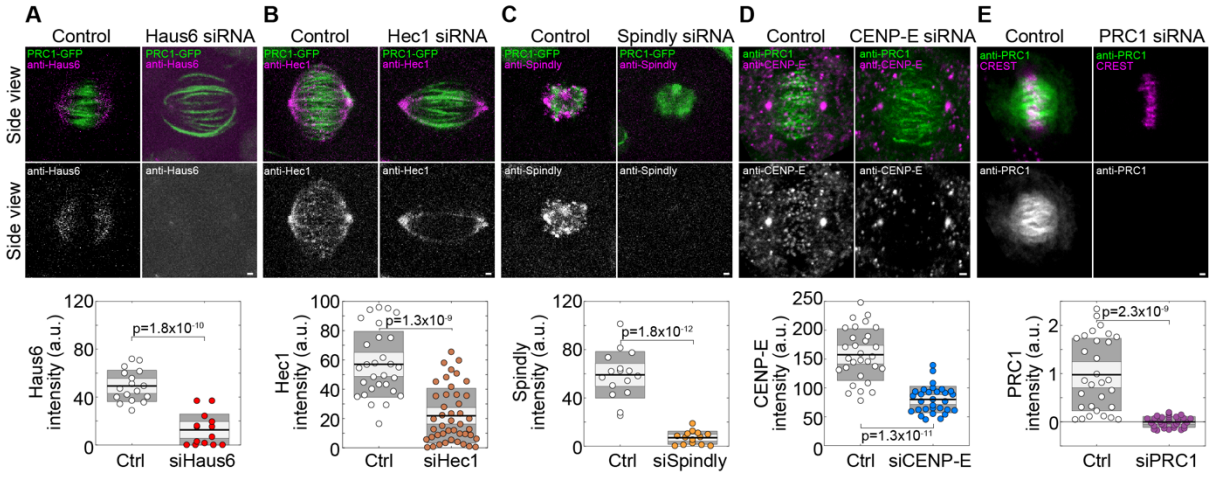

Extended Data Fig. 4: Quantification of protein depletion by immunostaining.

In each panel the images show control and depleted spindles, as indicated, with merged channels in the first row and only the channel of the depleted protein (white) in the second row. The graph under the images shows the quantification of the total signal intensity of the indicated protein on the spindle in control and depleted cells. For Hec1 depletion and the corresponding control, the total intensity of anti-Hec1 signal was measured in a region encompassing all DNA, i.e., excluding the poles. In **a-c**, HeLa-Kyoto BAC cell line stably expressing PRC1-GFP was used, whereas in **d**,**e**, untransfected HeLa cells were used. The number of cells was: (**a**) control, n=17, and Haus6 depletion, n=14, (**b**) control, n=29, and Hec1 depletion, n=44, (**c**) control, n=16, and Spindly depletion, n=14, (**d**) and (**e**), n=30 for each condition. Mean silencing was: (**a**) 74%, (**b**) 62%, (**c**) 90%, (**d**) 51%, (**e**) ~100% when the background signal is subtracted (data shown in panel **e**) and 86% without background subtraction (data not shown). In all control experiments the cells were transfected with nontargeting siRNA. All scale bars, 1 µm.

Supplementary Figure 5

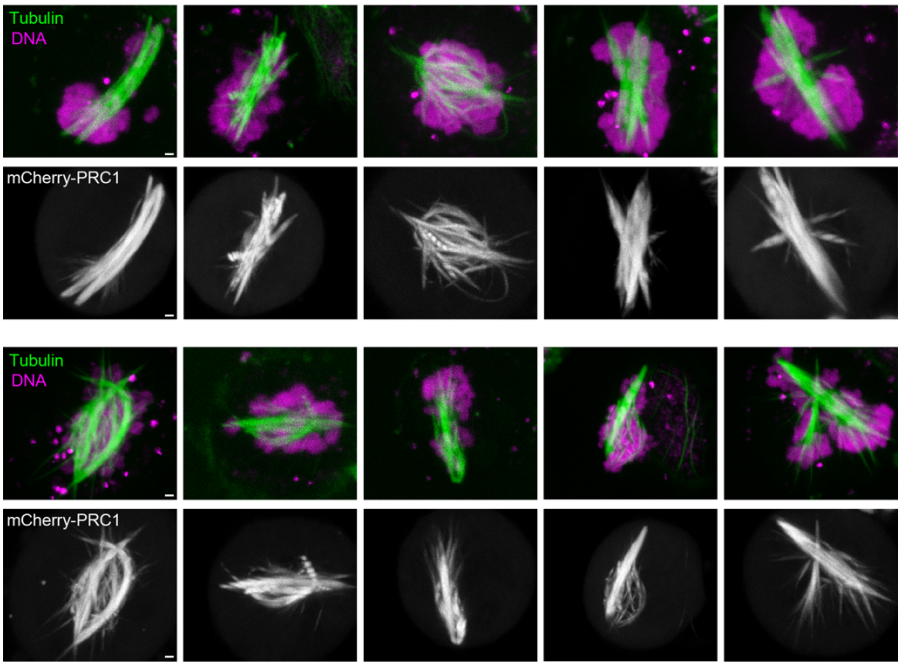

Extended Data Fig. 5: Additional images of spindles in cells with overexpressed PRC1. Examples of 10 spindles with overexpressed PRC1 in HeLa-TDS cells. Merged images show microtubules (SiR-tubulin, green) and DNA (Hoechst 33342, magenta), and the corresponding single-channel images below the merged ones show PRC1-mCherry (white). Scale bars, 1 µm.

1314 **SUPPLEMENTARY VIDEOS**

1315

1316 **Supplementary Video 1. Overlap bundle formation during early prometaphase.**
1317 Time lapse of a midplane of a vertically oriented prometaphase spindle in a HeLa-Kyoto BAC
1318 cell stably expressing PRC1-GFP starting with prometaphase rosette. A single plane is shown.
1319 Time interval between acquired images is 5.4 seconds. Time is shown in minutes:seconds.
1320 Scale bar, 1 µm.

1321

1322 **Supplementary Video 2. Bundle formation after Haus6 (augmin subunit) depletion.**
1323 Time lapse of a midplane of a vertically oriented prometaphase spindle in a Haus6-depleted
1324 HeLa-Kyoto BAC cell stably expressing PRC1-GFP starting with prometaphase rosette. A
1325 single plane is shown. Time interval between acquired images is 5.4 seconds. Time is shown
1326 in minutes:seconds. Scale bar, 1 µm.

1327

1328 **Supplementary Video 3. Bundle formation after Aurora B inhibition.**
1329 Time lapse of a midplane of a vertically oriented prometaphase spindle in a HeLa-Kyoto BAC
1330 cell stably expressing PRC1-GFP starting with prometaphase rosette. Barasertib was added just
1331 before the beginning of the movie. A single plane is shown. Time interval between acquired
1332 images is 5.4 seconds. Time is shown in minutes:seconds. Scale bar, 1 µm.

1333

1334 **Supplementary Video 4. Bundle formation after CENP-E inhibition.**
1335 Time lapse of a midplane of a vertically oriented prometaphase spindle in a HeLa-Kyoto BAC
1336 cell stably expressing PRC1-GFP starting with prometaphase rosette. GSK923295 was added
1337 just before the beginning of the movie. A single plane is shown. Time interval between acquired
1338 images is 5.4 seconds. Time is shown in minutes:seconds. Scale bar, 1 µm.

1339

1340 **Supplementary Video 5. Movement of overlap bundles during prometaphase.**
1341 Left, time lapse of a midplane of a vertically oriented prometaphase spindle in a HeLa-Kyoto
1342 BAC cell stably expressing PRC1-GFP starting with prometaphase rosette. The images were
1343 translated so that the position of the two bright bundles that are initially found in the upper
1344 region of the spindle is roughly constant. A single plane is shown. Time interval between
1345 acquired images is 2.7 seconds. Right, trajectories of the bundles from the movie on the left.
1346 Time is shown in minutes:seconds. Scale bar, 1 µm.

1347

1348 **Supplementary Video 6. Chromosome congression to the spindle midplane causes spindle**
1349 **widening, end-on view.**
1350 Time lapse of the central part of a vertically oriented prometaphase spindle in a HeLa-Kyoto
1351 BAC cell stably expressing PRC1-GFP (green) starting with prometaphase rosette. DNA is
1352 stained with SiR-DNA (magenta). Maximum projection of 3 middle planes is shown. Time
1353 interval between acquired images is 30 seconds. Time is shown in minutes:seconds. Scale bar,
1354 1 μm.
1355
1356 **Supplementary Video 7. Chromosome congression to the spindle midplane causes spindle**
1357 **widening, side view.**
1358 Time lapse of a horizontally oriented prometaphase spindle in a HeLa-Kyoto BAC cell stably
1359 expressing PRC1-GFP (green) starting with prometaphase rosette. DNA is stained with SiR-
1360 DNA (magenta). Sum of 41 planes is shown. Time interval between acquired images is 30
1361 seconds. Time is shown in minutes:seconds. Scale bar, 1 μm.